Cell Reports
Physical Science

Article

Chemical activity-based carbon-deposition risk maps for solid oxide fuel cell systems with off-gas recirculation

Graphical abstract

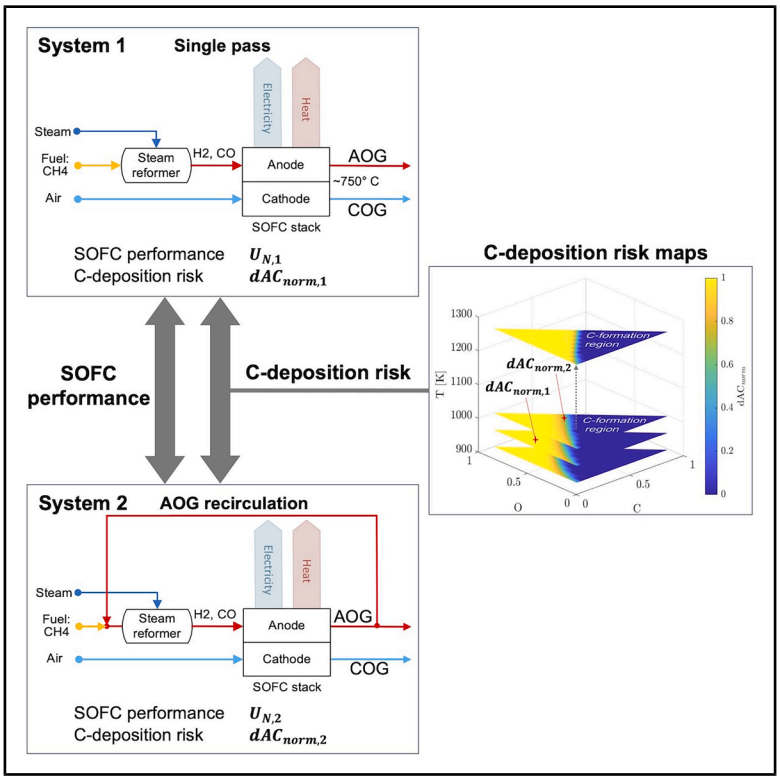

Highlights

- C-formation risk quantification methodology in C-H-O mixtures via chemical activity
- General 2D and 3D C-formation risk maps applicable to all hydrocarbon systems
- Comparison of normalized chemical activity with conventional risk metrics (SCR/OCR)
- Assessment of trade-off between C-deposition risk mitigation and SOFC performance

Authors

Victoria He, Arata Nakajo, Mar Pérez-Fortes, Jan Van herle, Jürg Schiffmann

Correspondence

victoria.he@epfl.ch

In brief

Carbon deposition, or coking, is a process that limits the operating window and lifetime of systems using hydrocarbon fuels. Existing C-formation indicators are overly simplistic, leading to incoherent recommendations for plant design and operation. He et al. thus present a more fundamental and coherent approach to quantify C-deposition risk.

He et al., 2026, Cell Reports Physical Science 7, 103106
February 18, 2026
https://doi.org/10.1016/j.xcrp.2026.103106

CellPress

Cell Reports
Physical Science

CellPress
OPEN ACCESS

Article

Chemical activity-based carbon-deposition risk maps for solid oxide fuel cell systems with off-gas recirculation

Victoria He,[1,5,*] Arata Nakajo,[2] Mar Pérez-Fortes,[3] Jan Van herle,[4] and Jürg Schiffmann[1]
[1]Laboratory for Applied Mechanical Design, Ecole Polytechnique Fédérale de Lausanne (EPFL), Lausanne, Switzerland
[2]European Commission, Joint Research Centre (JRC), Petten, the Netherlands
[3]Faculty of Technology, Policy and Management, Delft University of Technology, Delft, the Netherlands
[4]Group of Energy Materials, Ecole Polytechnique Fédérale de Lausanne (EPFL), Lausanne, Switzerland
[5]Lead contact
*Correspondence: victoria.he@epfl.ch
https://doi.org/10.1016/j.xcrp.2026.103106

SUMMARY

Here, we present a methodology for the generalized quantification of the carbon (C)-formation risk in hydrocarbon mixtures based on the normalized chemical activity. An open-source computational thermodynamics tool is coupled to a solid oxide fuel cell (SOFC) stack model to apply and validate this approach with literature data based on methane-fueled SOFC systems with anode off-gas recirculation. Two- and three-dimensional C-formation risk maps valid for all C-H-O mixtures are proposed for a practical, accurate, and meaningful assessment of the trade-off between C-deposition risk and SOFC performance. Compared to conventional risk evaluation methods such as steam-to-carbon ratio (*SCR*), oxygen-to-carbon ratio (*OCR*), or C-H-O ternary-phase diagrams, this approach allows a system-agnostic evaluation of different designs operated at varying conditions at a constant C-formation risk margin. The generalized formulation allows integration into process optimization workflows to obtain high-performance system designs with extended stack operating windows.

INTRODUCTION

Solid oxide fuel cell (SOFC)-based systems are one promising renewable energy technology on the verge of commercial viability. They provide electricity and heat from the electrochemical conversion of fuel and O_2 at high temperature, typically 500°C–800°C for the so-called intermediate temperature (IT) SOFC technology.[1–3] Fuels of practical relevance include natural gas (a mixture of CH_4, C_2H_6, and/or CO_2[4,5]), syngas (H_2 and CO[6,7]), and biogas (CH_4 and CO_2[8]), all of which consist of the components H, C, and O. A supply of steam is required in most situations where an SOFC-based system runs on such hydrocarbon fuels for re-formation.[9]

The highest stand-alone SOFC system efficiencies are usually reached near the limits of the SOFC stack operating window, e.g., at the highest fuel utilization ratios (increasing electrical efficiency based on the lower heating value of the fuel at the risk of fuel starvation and anode oxidation[10]) and the lowest steam content and pre-re-forming fractions (increasing overall efficiency from reduced external steam requirements, energy expenses for the re-former, and balance of plant at the risk of thermal degradation and carbon (C) deposition[11,12]). Exceeding the stack operating window leads to material degradation, reduced lifetime, and reduced SOFC performance, which negatively affect the system performance and economic viability.[13,14] Therefore, advances in understanding and increasing prediction accuracy of safe operating conditions are paramount for enhancing the long-term performance of fuel cell systems.

One of the processes that restrict the operation of the system with hydrocarbon fuels is the chemical formation and deposition of solid carbon in the SOFC stack.[12] The thermodynamic and kinetic conditions for the conversion of part of the fuel via undesirable chemical side reactions that form solid carbon structures may be reached locally. Solid graphite, which consists of weakly bound layers of graphene stacked in a hexagonal crystalline structure, is thermodynamically stable in the temperature and pressure ranges of IT-SOFC systems (around 1–3 atm and 650°C–800°C) and can be produced by catalytic decomposition via the Boudouard reaction or thermal cracking.[15] Carbon whiskers or nanotubes are other commonly formed solid carbon structures that are produced from interactions between the fuel and a catalyst. Their morphology is a specific conformation of graphene layers coupled to a metallic catalyst particle, such as nickel.[16–18] These carbon structures drastically decrease the density of effective catalytic and electrocatalytic sites by covering the anode-pore interface and may lead to structural and morphological changes in the anode material. In addition, clogging of the distribution channels limits the gas-phase transport and inhibits the electrocatalytic properties of the electrode. As a consequence, the cell performance and

Please cite this article in press as: He et al., Chemical activity-based carbon-deposition risk maps for solid oxide fuel cell systems with off-gas recirculation, Cell Reports Physical Science (2026), https://doi.org/10.1016/j.xcrp.2026.103106

lifetime decrease significantly, as extensively reported in the literature.[12,19–21]

Recirculation of part of the anode off-gas (AOG) from the fuel cell outlet is a possibility to avoid coking and additionally circumvents the complexity and costs of steam generation in the system by using the steam produced by the electrochemical oxidation of H_2 for fuel re-forming.[22–28] However, high AOG recirculation ratios (*RR*s) have also been found to decrease the stack performance in terms of voltage output due to fuel dilution depending on the operating conditions (e.g., used fuel, re-forming requirements, and full- or part-load operation).[23,25,29] Current understanding of the trade-offs between C-deposition mitigation, system simplification, changes in fuel composition, and flow distribution, among others, remains imprecise. AOG recirculation experiments are complex, seldom fully controllable (highly interdependent parameters and components[30]), or even unfeasible (limited availability of suitable high-temperature recirculation devices off the shelf). In fact, most experimentally reported AOG recirculation tests were determined with a synthetic AOG mixture in a single-pass SOFC system.[26,31–33] These limitations lead to uncertainties that can mask the actual trends and effects of AOG recirculation on the stack and system performance, preventing the establishment of generalized guidelines for system design and safe operation.

In current practice, safe operating conditions to avoid coking are assessed using metrics such as steam-to-carbon ratio (*SCR*) and oxygen-to-carbon ratio (*OCR*), with thresholds and safety margins based on *a priori* inspection of C formation isotherms in C-H-O ternary-phase diagrams calculated using literature data or computational thermodynamics software (Calculation of Phase Diagrams—CALPHAD).[34–38] Such practical approaches allow straightforward estimations of the C-deposition risk but have significant limitations.

First, their outcome is not unequivocal, as exceptions to fixed threshold rules are not uncommon. For methane-fueled SOFC systems, differing safe threshold values against C formation have been reported compared to the commonly applied value of $SCR = OCR = 2$ (stochiometric for steam methane re-forming): Halinen et al.[32] did not experimentally detect significant C deposition for $SCR = 0.53$ in the pre-re-former at temperatures of 646°C in an SOFC system with AOG recirculation and suggested in another publication[39] a minimum $OCR = 1.5$ for temperatures above 650° as a criterion to avoid C deposition, which is lower than the threshold Peters et al.[40] recommended (minimum $OCR = 2.3$ at 500°C). Then again, Tsai et al.[41] experimentally found that C formation occurred even for $OCR > 1.5$ under SOFC internal methane re-forming conditions. This highlights that generalized conclusions are difficult using the simplistic *SCR* and *OCR* metrics, as they do not reflect physical parameters that strongly affect C formation, such as the used fuel, catalyst, operating temperature, residence time, or extent of the thermodynamic equilibrium. Fuel-cell-specific parameters have also been found to influence C formation, such as the anodic polarization.[42]

Second, the C-deposition risk can be evaluated only in a binary way (with C deposits either forming or not) over the position of the operating point relative to the thermodynamic C-formation boundary. This binary risk assessment skews performance comparisons, as the margin to the C-formation threshold (e.g., expressed by different grades of fuel dilution) is not quantifiable, yet it still impacts the SOFC performance. Tanaka et al.[31] conducted CH_4-fed single-cell tests and compared the SOFC operated under single-pass conditions ($SCR = 2.5$ to avoid C deposition) with AOG recirculation conditions (simulated AOG, $RR = 0.67$) at constant FU_{sys} of 0.9. They found that AOG recirculation leads to an improved stack performance or cell voltage while still avoiding C formation. Under similar operating conditions (constant $FU_{sys} = 0.9$, CH_4-fed single cell, simulated AOG), Terayama et al.[26] also reported an increase in the cell voltage under AOG recirculation conditions ($RR = 0.7$) compared to single-pass operating conditions ($SCR = 2–3$). Similar observations have been reported by Wagner et al.,[43] who tested an SOFC stack with AOG recirculation at constant $FU_{sys} = 0.7$ and varying *RR* and found an increase in the cell voltage for $RR = 0.474$ compared to the single-pass case ($SCR = 2.1$). However, none of the authors evaluated whether the single-pass operating conditions were excessively diluted from the outset given the different safe thresholds or *SCR* used. More conclusive results would have been obtained if the comparisons between single-pass and AOG recirculation modes were made at constant safety margins or C-deposition risk levels, which is not possible using the conventional risk assessment methods.

Instead, a better parameter to quantify the risk of solid C formation in SOFC systems during the conceptual design phase can be the chemical activity, since it expresses the tendency of a species to undergo a chemical reaction or a phase change—provided a consistent choice of standard state (usually at 1 bar and 298.15K). Further, the chemical activity is a dimensionless and a measurable quantity (via, e.g., mass spectrometry[44] or galvanic cells[45]), since it directly relates to the chemical potential and thus to the Gibbs energy. Therefore, research groups have worked on improving C-H-O ternary-phase diagrams, such as using approaches from the field of metallurgy[46] via the integration of iso-activity lines of various carbon allotropes[47] or iso-activity lines as a function of pressure.[48] Others have focused on the identification of the effects of different SOFC operating parameters (such as temperature, pressure, or *FU*) on activity as an indicator of C formation in the form of graphite.[27,49] However, to the best of our knowledge, studies using carbon activity as a physical parameter to evaluate and compare SOFC performance under different operating conditions, e.g., with and without AOG recirculation with a constraint of constant safety margin for C deposition, are not available in the literature.

In this article, we propose a method to assess and quantify the C formation risk based on chemical activity as a physical and measurable parameter. For this, the open source computational thermodynamics tool OpenCalphad is coupled to an existing thermoelectrochemical SOFC stack model for the combined assessment of the C-formation risk and the SOFC performance. The established SOFC-OpenCalphad model is validated using selected literature cases involving methane-fueled SOFC systems with and without AOG recirculation. Further, the model is applied to gain an in-depth and systematic understanding of the effect of AOG recirculation on the C-deposition risk and cell performance in planar anode-supported SOFC stacks.

Table 1. Selected literature cases for model validation

Case	Reference	SOFC system	Cell support	Analysis	AOGR method	Risk metric
Case 1	Henke et al.[22]	planar, stack	anode	numerical	–	T_{Cdep}
Case 2	Liu et al.[25]	tubular, stack	cathode	experimental	ejector	$OCR > 2.2$
Case 3	Terayama et al.[26]	planar, single cell	anode	experimental	single pass, emulated AOG	SCR, T_{Cdep}
Case 4	Baba et al.[24]	tubular, stack	cathode	experimental	ejector	$OCR > 2$, phase diagram

Generalized and comprehensive guidelines as well as C-formation risk maps valid for all C-H-O compositions are established that facilitate the exploration of innovative design solutions and the extension of safe operating windows with regard to C deposition.

RESULTS

Effect of AOG recirculation on C-deposition risk

To ensure model and results generalizability, the SOFC-OpenCalphad model has been validated and applied to a selection of four literature cases that cover different methane-fueled IT-SOFC system (planar or tubular) and cell (anode- or cathode-supported) types, AOG recirculation conditions (emulated or actual AOG recirculation), evaluation methods (numerical or experimental), and C-deposition risk assessment metrics (*SCR*/*OCR*, C-deposition temperature, or ternary diagrams) (see Tables 1 and 2).

The C-deposition risk assessment for the operating conditions given in the published data is carried out by determining the chemical activities, as introduced in Equation 19, for the comparison of the safe operating ranges given in the literature. The parameters used for the risk assessment are defined in the methods, and the conditions used are taken from the literature cases and summarized in Table S1. For all literature cases, the C-deposition risks obtained over different *RR* at constant FU_{sys} are shown in Figure 1A.

Case 1

Henke et al.[22] mention that the C-deposition boundary depends highly on the operating pressure, temperature, and fuel and that AOG recirculation reduces the risk of C formation of the SOFC system, keeping the effect on performance outside of the discussion. The C-deposition risk assessment via carbon activity of case 1 indicates that, at the inlet operating conditions used (see Table 2), a minimum *RR* of 0.525, 0.38, and 0.36 is required for FU_{sys} of 0.6, 0.75, and 0.9, respectively, to avoid solid graphite formation (C deposition when $dAC_{norm} = 0$) (see Figures 1A and S1A). At temperatures of 550°C, the minimum *RR* that is required to avoid C deposition is 0.66 and 0.57 for an FU_{sys} of 0.75 and 0.9, while there is no risk of C deposition for an FU_{sys} of 0.6 for all *RR*. Compared to their given safe operating limit at 550°C of minimum *RR* of 0.7 and 0.58 at $FU_{sys} = 0.75$ and 0.9 (see Figure 2 of Henke et al.[22]), these limits suggest similar, at most slightly larger, safe operating limits for the investigated planar anode-supported stack as proposed.

Case 2

Liu et al.[25] suggest an $OCR > 2.2$ as a safe threshold to prevent C deposition and concluded that AOG recirculation decreases the C-deposition risk. However, the determined C-deposition risk based on chemical activity for *OCR* of 2.2 using the operating conditions of case 2 is $dAC_{norm} = 0.87$, representing a safety margin for the C-formation limit of 87%. This indicates that there still is a large buffer to the operational threshold for the investigated tubular cathode-supported stack—even for *OCR* as low as 1.4 ($dAC_{norm} > 0$), as shown in Figures 1A and 8B.

Case 3

The analysis by Terayama et al.[26] in the light of *SCR* showed that increasing recirculation reduces the C-deposition risk in the re-former. They proposed an *RR* of $\geq$0.6 to avoid C deposition in the re-former (which operates between 873K and 973K) at the

Table 2. Input conditions used for the SOFC-OpenCalphad model to replicate literature cases

Case	Reference	Name	p_{in} (bar)	$T_{air,in}$ (K)	$T_{CH4,in}$ (K)	FU_{sys} (–)	j_{avg} ($A\ cm^{-2}$)	$T_{PEN,max}$ (K)	*RR* (–)
Case 1	Henke et al.[22]	$FU = 0.6$	1.013	973*	973*	0.6	0.4*	1,043*	0.21–0.735
		$FU = 0.75$	1.013	973*	973*	0.75	0.4*	1,043*	0.163–0.87
		$FU = 0.9$	1.013	973*	973*	0.9	0.4*	1,043*	0.151–0.85
Case 2	Liu et al.[25]	$FU = 0.8$	1.013	993	997*	0.8	0.31–0.75*	1,183	0.437–0.754
Case 3	Terayama et al.[26]	$FU = 0.9$	1.013	1,003[a]	1,003[a]	0.9	0.2*	1,043[a]	0.42–0.8
		$FU = 0.8$	1.013	1,003[a]	1,003[a]	0.8	0.2*	1,043[a]	0.4–0.8
		$FU = 0.7$	1.013	1,003[a]	1,003[a]	0.7	0.2*	1,043[a]	0.4–0.8
Case 4	Baba et al.[24]	load 100%	1.013	853	993	0.84	0.249*	1,114*	0.667–0.714
		load 80%	1.013	853	993	0.84	0.2*	1,157*	0.595–0.68
		load 70%	1.013	853	993	0.84	0.174*	1,133*	0.631–0.694
		load 62.5%	1.013	853	993	0.84	0.156*	1,121*	0.63–0.677

*Not provided explicitly and thus inferred through inverse modeling to replicate literature plots.
[a]Approximated such that average T_{SOFC} = 1,023*K*, as given in original source.

Please cite this article in press as: He et al., Chemical activity-based carbon-deposition risk maps for solid oxide fuel cell systems with off-gas recirculation, Cell Reports Physical Science (2026), https://doi.org/10.1016/j.xcrp.2026.103106

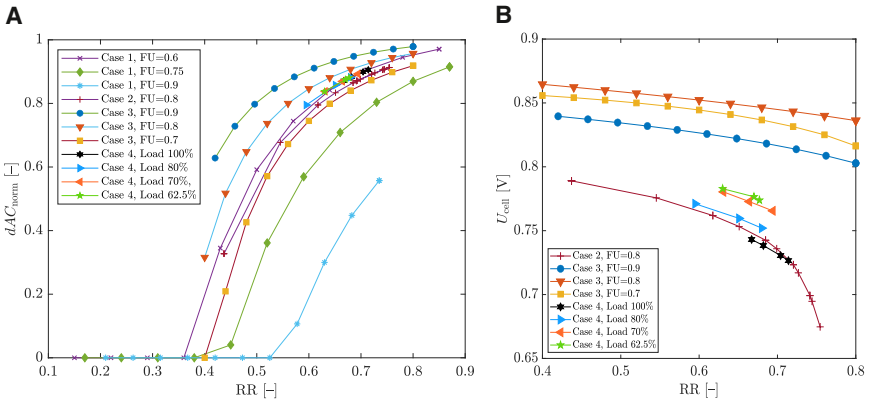

Figure 1. C-deposition risk and SOFC performance over *RR* in literature cases

Determined at constant p_{in} = 1 atm using the SOFC-OpenCalphad model with conditions based on Tables 2 and S1.

(A) dAC_{norm} over *RR* for cases 1–4.

(B) U_{cell} over *RR* for cases 2–4.

FU_{sys} of 0.9. This represents a C-deposition risk of dAC_{norm} = 0.33 or a safety margin for the C-formation limit (dAC_{norm} = 0) of 33%. This means that there still is a potential for the expansion of the operating limits. The minimum *RR* required to avoid C deposition in the re-former has been determined to >0.5 for FU_{sys} = 0.9 at the temperature of 873K, which represents a deviation by 16.7% from the proposed *RR*.

Further, according to Terayama et al.,[26] the highest anode-supported single-cell efficiency within the considered FU_{loc} range is expected for FU_{sys} of 0.9, at which the C-deposition temperature is the lowest. The carbon activities have been calculated using the operating conditions of case 3 (see Table 2), showing that for FU_{sys} = 0.8 and 0.9, no C deposition would occur in the SOFC even for *RR* as low as 0.4, while for FU_{sys} = 0.7, the minimum *RR* to avoid C deposition should be higher than 0.4 (dAC_{norm} = 0) (see Figures 1A and S1B).

Case 4

Baba et al.[24] have shown that, under their tested conditions, AOG recirculation without an external water supply for steam re-forming did not lead to C deposition. They did not provide an *RR* limit for safe operation but investigated the effect of full-load and part-load operation in combination with AOG recirculation on the SOFC performance. Using the operating conditions of case 4 (see Table 2), the determined C-deposition risks at constant *RR* for full- and part-load operation have a high degree of similarity, signifying that, for the investigated tubular cathode-supported stack, the C-deposition risk is, in fact, not affected by the mode of operation (see Figures 1A and S1C).

Local C-deposition risk

The C-deposition risk can also be assessed locally within the stack by taking into account gas composition and temperature changes in the flow direction along the gas channel $y_{gaschannel}$. Due to the continuous electrochemical conversion of the fuel along the gas channel, the temperature rises (exothermal reaction), while the anode-side gases become increasingly diluted with CO_2 and H_2O—leading to the highest fuel dilution and temperatures at the stack outlet. With this behavior, and following Equations 2 and 19, the maximum local C-deposition risk can be expected at the stack inlet and the minimum at the stack outlet. This has been confirmed for all literature cases using the SOFC-OpenCalphad model, where at constant *RR*, the local C-deposition risk decreases in flow direction along the gas channel $y_{gaschannel}$ (see Figure S2). Notably, varying load conditions at constant FU_{sys} and *RR* do not significantly affect the local C-deposition risk distribution in case 4 (some overlap in dAC_{norm} in Figure S2D).

All investigated cases and thus SOFC system and cell types (see Figures 1A and S2) have in common that, for increasing *RR*, the C-deposition risk decreases ($dAC_{norm} \rightarrow 1$), especially at the stack inlet, due to the increased fuel dilution from the recirculated reaction products CO_2 and H_2O. Further, at constant *RR*, decreasing the FU_{sys} increases the overall C-deposition risk within the stack ($dAC_{norm} \overrightarrow{\rightarrow 0}$) (lower fuel conversion within the cell, hence less fuel dilution along the gas channels; see Equation 23). Following the trends of dAC_{norm} in Figure 1A, a certain amount of *RR* (or, as an alternative, of H_2O injection) is required to avoid C deposition in all considered cases at their respective operating conditions.

Finally, the C-deposition safety limits based on the conventional metrics (*SCR*, *OCR*, T_{Cdep}, and C-H-O ternary diagrams) proposed in the literature cases for the different SOFC system and cell types appear overly conservative, with large margin variations, leaving room to safely extend the operating range of SOFC.

Effect of AOG recirculation on SOFC performance

The effects of AOG recirculation on the SOFC performance are assessed under the known operating conditions from the literature, using the Nernst potential (see Equation 24). Since a direct comparison with the SOFC performance data from the literature cases is limited due to incomplete information on SOFC geometry and operating conditions, the SOFC performance is calculated here on the basis of the planar SOFC geometry used in the thermoelectrochemical model and the conditions from Table 2 that are used to match the literature results. This allows a comparison of the trends and behavior of the SOFC performance as a function of the AOG *RR* in relative terms for anode-supported planar cells. As Henke et al.[22] did not discuss the SOFC performance in their work (case 1), the focus here is placed on cases 2–4.

Case 2

Liu et al.[25] compared the effects of AOG recirculation for a syngas-fueled SOFC system only, where they found that AOG recirculation led to a penalty on the SOFC net electrical efficiency as

high as 20% compared to a single-pass system without AOG recirculation. For the CH_4 fueled system, they determined a penalty in the SOFC cell voltage at 22.4% with increasing *RR* from 0.437 to 0.674 (see Figure 8 in Liu et al.[25]). This behavior was also detected with the SOFC-OpenCalphad model with CH_4 as fuel under the conditions of Table 2, where, with increasing *RR* from 0.437 to 0.674, the cell voltage decreases by 14.5% (see Figure 1B), owing to the increasing fuel dilution (and, as a side note, a lower C-deposition risk) with increasing *RR* and thus lowering the Nernst potential U_N (Equation 24).

Case 3

Using the operating conditions from Table 2 and the proposed model, a penalty in SOFC performance with increasing *RR* was also found for case 3. With increasing *RR* from 0.4 to 0.8, the cell voltage drops by 4.6% and 3.28%, for FU_{sys} of 0.7 and 0.8, and by 4.38% for FU_{sys} = 0.9 (*RR* = 0.42–0.8) (see Figure 1B). Interestingly, Terayama et al.[26] reported up to 6.4% higher electrochemical performance of the system with AOG recirculation (FU_{sys} = FU_{loc} = 0.9, j_{avg} = 0.46 cm^2, and *RR* = 0.7) compared with the single-pass cases without recirculation (FU_{sys} = FU_{loc} = 0.9, j_{avg} = 0.46 cm^2, *RR* = 0, and *SCR* = 2–3), despite the gas composition at the anode inlet being more diluted for the AOG recirculation case than for the single-pass cases (see Table 2 of Terayama et al.[26]). This behavior seemingly contradicts the results of case 2 and those obtained with the SOFC-OpenCalphad model. Terayama et al.[26] reason that the AOG composition leads to a lower area-specific resistance, which compensates for the lower U_N from the fuel dilution, thus achieving a higher cell voltage than the single-pass cases. However, their comparison is flawed, since they did not implement actual AOG recirculation tests but used externally supplied gases to mimic the AOG composition under *RR* = 0.7 conditions at the anode inlet, while keeping the FU_{loc} constant at 0.9. However, this would in reality lead to a system fuel utilization of FU_{sys} = 0.968 (Equation 22), which is significantly higher than the *FU* of the single-pass cases (FU_{sys} = 0.9)—resulting in higher SOFC performance despite the fuel dilution from AOG recirculation.

For a better comparison, the AOG recirculation and single-pass cases should be considered at constant FU_{sys} as done in the other literature cases. When AOG is recirculated, FU_{loc} has therefore to be lowered (see Equation 22) to keep the FU_{sys} constant; here, for *RR* = 0.7, the local fuel utilization ratio should be set to FU_{loc} = 0.73 to achieve constant FU_{sys} = 0.9. Under these adjusted operating conditions and using the SOFC-OpenCalphad model, it becomes clear that AOG recirculation at *RR* = 0.7 leads to a worse SOFC performance when compared with single-pass cases of *SCR* = 2–3—even though the single-pass case *SCR* = 3 is showing a slightly lower C-deposition risk and thus a slightly higher grade of fuel dilution (see Table S2). This indicates that the recirculation of CO_2 and H_2O is more detrimental to the cell performance than the single-pass case with varying *SCR* (fuel dilution from H_2O only).

Case 4

The analysis of Baba et al.[24] suggests that AOG recirculation has a detrimental effect on the SOFC performance under full-load operation due to fuel dilution. In contrast, the SOFC power output remained unaffected during part-load operation between 62.5% and 80% and for the tested *RR*s between 0.595 and 0.694, while the C-deposition risk is decreased. However, using the SOFC-OpenCalphad model, a penalty on the cell voltage was also detected under the part-load operating conditions, where, with increasing *RR* from 0.667 to 0.714, the cell voltage dropped by 2.22% (see Figure 1B). One reason for this discrepancy could be the current SOFC model being established for planar cells, while Baba et al.[24] were using a tubular cell in their investigations.

It becomes clear for the investigated conditions that the SOFC performance decreases with increasing AOG *RR*—the main reason being the fuel dilution: The recirculation of AOG, which contains both H and C components, leads to a stronger fuel dilution than in the single-pass cases, where only the H content increases with increasing H_2O injection—lowering the Nernst potential U_N. However, the AOG recirculation effect on the SOFC performance depends highly on the cell (e.g., anode or cathode supported and geometry) and stack type (e.g., planar or tubular) as well as the shares of overpotentials from activation, ohmic, and diffusion losses: as Terayama et al.[26] have pointed out, a lower overpotential under certain conditions could help to compensate for the penalty on the Nernst potential U_N. It is to be noted that, since the information on the SOFCs used in the literature cases is incomplete and the thermoelectrochemical SOFC model used has been validated for planar anode-supported SOFCs, the penalty on the cell voltage from AOG recirculation presented here is representative of commercial anode-supported planar SOFCs only.

Maps for C-deposition risk and fuel cell performance

For a generalized comparison of the trade-off between C-deposition risk mitigation and SOFC performance, we generated a 3D map using the SOFC-OpenCalphad model that allows a simple and fast quantification of the C-deposition risk (dAC_{norm}) for C-H-O ternary systems at constant pressure and varying temperatures: Figure 2 shows iso-dAC_{norm} surfaces (natural neighbor interpolation) for dAC_{norm} = 0.1–0.9 at 1 atm across the temperature range of 873K–1,273K over the logarithmic axes of C and O (H = 1 − C − O). C-H-O compositions where dAC_{norm} = 0 or 1 are excluded for better visibility, since they do not form iso-dAC_{norm} surfaces but iso-dAC_{norm} volumes. For low temperatures, the iso-dAC_{norm} surfaces are spaced apart, thus indicating differing C-deposition risks depending on the C-H-O composition. As the temperature increases, the iso-dAC_{norm} surfaces seem to converge into one line, indicating that the C-deposition risk assessment tends to a binary classification under these conditions. This can be explained by the increasing reaction rates with temperature, making the thermodynamic equilibrium more susceptible to slight changes in gas composition. Consequently, the proposed 3D C-deposition risk map enables effective and systematic comparisons between different SOFC operating conditions at constant risk level.

At constant temperatures, the normalized carbon activity dAC_{norm} spans a continuous surface for different C-H-O compositions, as shown exemplarily for *T* = 973K in Figure S3. For better visualization and use, we therefore propose 2D maps for the visualization of the iso-dAC_{norm} curves over the C and O axes (H = 1 − C − O) for ternary C-H-O systems. These 2D maps allow

Please cite this article in press as: He et al., Chemical activity-based carbon-deposition risk maps for solid oxide fuel cell systems with off-gas recirculation, Cell Reports Physical Science (2026), https://doi.org/10.1016/j.xcrp.2026.103106

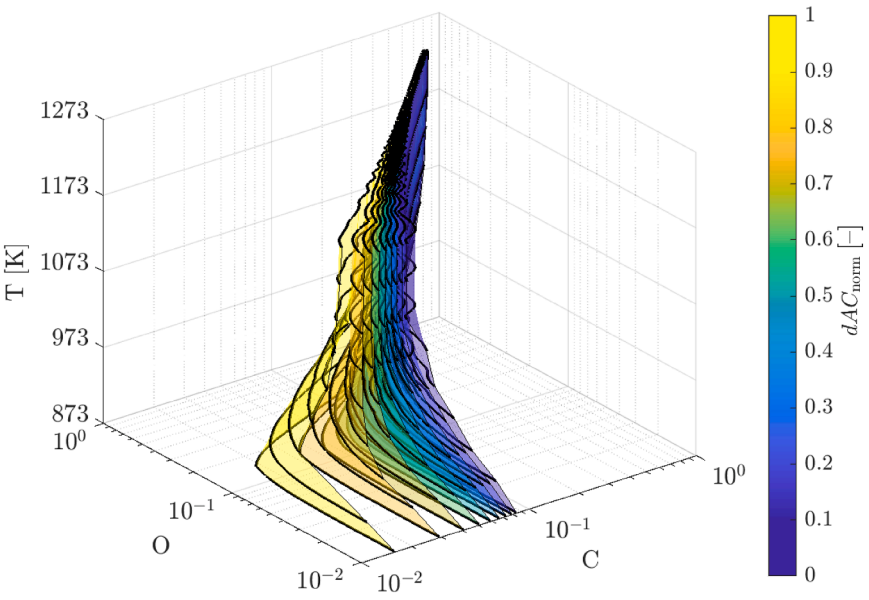

Figure 2. Three-dimensional iso-dAC_{norm} maps for ternary C-H-O systems under different operating temperatures at constant p = 1 bar

Log-scale for C and O, with H = 1 − C − O. C formation at dAC_{norm} = 0. Contour undulations due to natural interpolation across more than 4,800 discrete C-H-O compositions per temperature step are shown.

for a better comparison between dAC_{norm} and the conventional risk assessment metrics across a range of C-H-O compositions and temperatures. In Figure 3, selected iso-*OCR* lines for the lower (873K) and upper operating limits (1,273K) of ambient IT-SOFC systems are shown, confirming that safety thresholds based on fixed, near stoichiometric *SCR* or *OCR* values (e.g., *SCR* = *OCR* = 2 for steam methane reforming [SMR]) are of limited reliability: depending on the operating point, they can be either overly conservative ($dAC_{norm} \rightarrow 1$), e.g., for low C contents and high temperatures, or insufficient ($dAC_{norm} \rightarrow 0$), e.g., for high C contents and low temperatures—showcasing the inconsistent and highly case-specific operational safety recommendations found in the literature. The proposed dAC_{norm} metric thus overcomes these limitations and enables generalized safety margin quantification, which in turn allows the formulation of system-independent operational recommendations.

The 2D iso-dAC_{norm} maps can further allow for a fast assessment of the trade-off between C-deposition mitigation and SOFC performance by incorporating iso-U_N points (see Figure 4). The iso-U_N points are determined with the thermoelectrochemical model for the SOFC inlet conditions of interest, excluding C-H-O compositions that lead to C deposition or that do not contain enough H components for the internal water gas shift, SMR, or electrochemical reactions. The trade-off assessment between C-deposition risk mitigation and SOFC performance is illustrated with case 1 (FU_{sys} = 0.9, T = 973K, and p = 1 bar, see Table 2): it can be observed that, with increasing *RR*, the operating points of case 1 shift toward higher dAC_{norm} values and lower U_N. The same effect can be seen with increasing *SCR* or *OCR* under single-pass conditions. However, at constant dAC_{norm}, it can be seen that AOG recirculation leads to a higher penalty on the SOFC performance than the single-pass case for CH_4-fueled anode-supported planar SOFC stacks.

Notably, the 2D map shows that the C-H-O region leading to the highest SOFC performance (maximum U_N) is located close to the C-formation limit ($dAC_{norm} \rightarrow 0$) and at low C and O values (bottom left corner of the map). With increasing C and O content, U_N decreases and the iso-U_N points converge into a single value. This indicates that, for gas compositions with a low C and O content (thus high H content), the SOFC performance is less sensitive toward a change in dAC_{norm} and thus less sensitive toward fuel dilution. Under these conditions, AOG recirculation has therefore little impact on the SOFC performance while achieving C-deposition mitigation, and the trade-off between the two aspects is small. In the case of CH_4-fueled SOFCs, it is therefore recommended, ideally and following intuition, to remove CO_2 from the AOG before its recirculation.

Additional 2D maps with iso-dAC_{norm} curves for different temperatures are shown in Figure 5. No iso-U_N points have been included there, since they depend on the operating conditions and type of fuel cell.

DISCUSSION

The developed SOFC-OpenCalphad model has been validated and compared with different literature cases, showing a high results agreement in the reproduced literature plots. The minor deviations from the literature data can be explained by the different C-H-O compositions approximated with the thermoelectrochemical model, as well as differences in the thermodynamic databases and computational thermodynamics software.

For the C-deposition risk assessment, the proposed iso-dAC_{norm} maps apply to all ternary systems independently of the investigated chemical or electrochemical system. The proposed maps have been generated by natural neighbor interpolation[50] across more than 4,800 calculated discrete C-H-O compositions per temperature step to achieve a good trade-off between accuracy and computational effort, with minor localized undulations introduced as a side effect. The accuracy and shape of the contour maps could thus be further improved by increasing the number of C-H-O compositions at the cost of higher runtime.

Further, it is to be noted that this paper treats the risk of C deposition as the thermodynamic formation of graphitic carbon. The effects of the reaction kinetics, further convoluted by the catalyst morphology and structure involved in the formation of other carbon allotropes such as carbon whiskers, are not

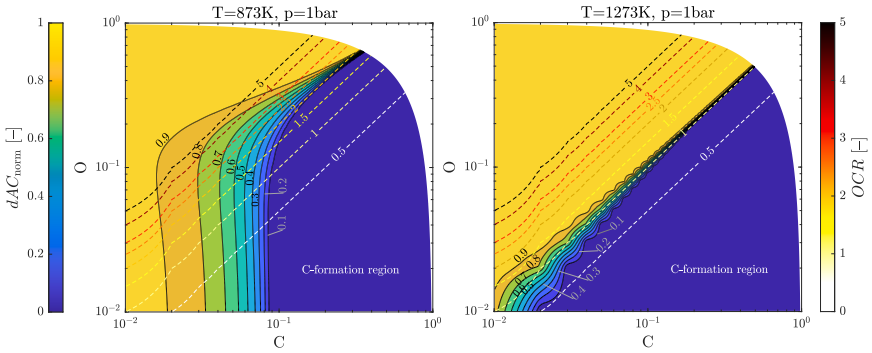

Figure 3. Two-dimensional iso-dAC_{norm}-C-O maps with iso-*OCR* lines at constant p = 1 bar for temperatures 873K and 1,273K

Log-scale for C and O, with H = 1 − C − O. C-formation region at dAC_{norm} = 0.

considered. Unlike surface-level graphitic carbon, which significantly reduces SOFC performance due to blockage of the active sites, carbon whiskers or nanotubes were not observed to lead to immediate performance loss (porous anode materials) but do affect SOFC lifetime due to irreversible morphological damage without possible regeneration of the affected structures.[15,16,18,21] Literature findings show complex and partly inconsistent behavior concerning the formation and spatial occurrence of such carbon allotropes, indicating highly case-specific behavior and current incomplete understanding of the involved kinetic effects, catalyst material, and morphology influences: Bartholomew[51] indicated the formation of carbon whiskers under steam re-forming conditions at temperatures above 450°C, 150K lower than for graphite (>600°C). Gozzi et al.[52] experimentally detected carbon nanotube formation from CH_4 decomposition at temperatures above 809K, which is only 10K below the graphite formation temperature. The same authors further found that solid graphite can thermodynamically transform to carbon nanotubes spontaneously at temperatures above 704K. The same phenomenon was also observed by Wang et al.,[53] who conducted long-term SOFC stack tests at 750°C, where, at increased operating time and severity of graphitic C deposition, carbon whiskers formed and destroyed the anode microstructure at the SOFC inlet. Lanzini et al.[20] experimentally investigated SOFC degradation under direct dry-re-forming conditions (*SCR* = 1) and detected carbon whisker formation mainly at the anode inlet. Subotic et al.[19] also conducted direct dry-re-forming tests (*SCR* = 0.5, 800°C), but found carbon nanofibers over the entire anode surface, with the majority of C formation at the anode outlet. Based on these findings, a practical recommendation is to apply more conservative safety margins ($dAC_{norm} \rightarrow 1$) than thermodynamically suggested under situations potentially promoting non-equilibrium conditions (e.g., during transient operation), such as via increased AOG *RR* or external steam injection. The safety margin can then be progressively reduced ($dAC_{norm} \rightarrow 0$ or $dAC_{norm} > 0$) with conditions approaching equilibrium. The proposed iso-dAC_{norm} maps facilitate the quantification of these safety margins and thus can guide operational optimization toward higher fuel cell performance and lifetime. For full detail safety margin assessments, incorporating reaction kinetics and morphological effects is expected to be necessary on a case-specific basis (depending

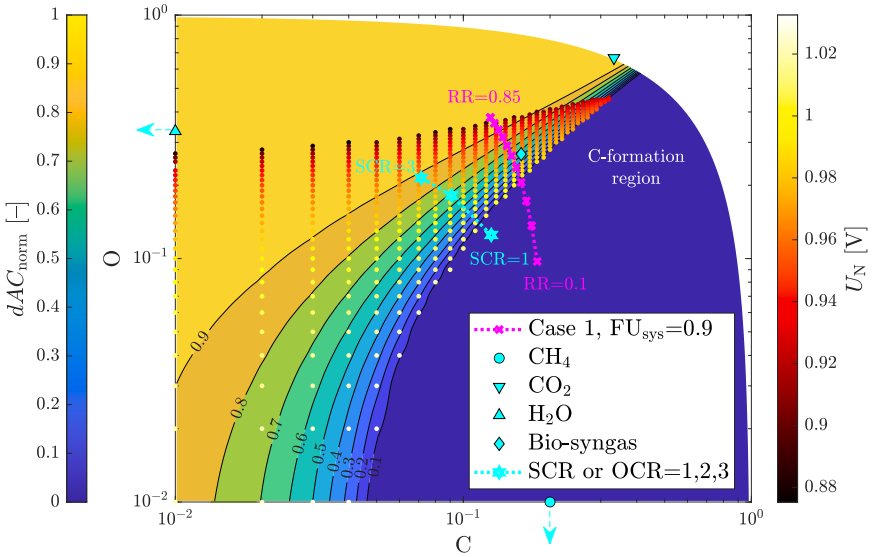

Figure 4. Two-dimensional iso-dAC_{norm}-C-O map at T = 973K, p = 1 bar with iso-U_N points determined for case 1

Log-scale for C and O, with H = 1 − C − O. Iso-U_N points for case 1 at FU_{sys} = 0.9 and j_{avg} = 0.4 A/cm^2 (see Table 2). C-formation region at dAC_{norm} = 0. Points outside of scale are marked with an arrow.

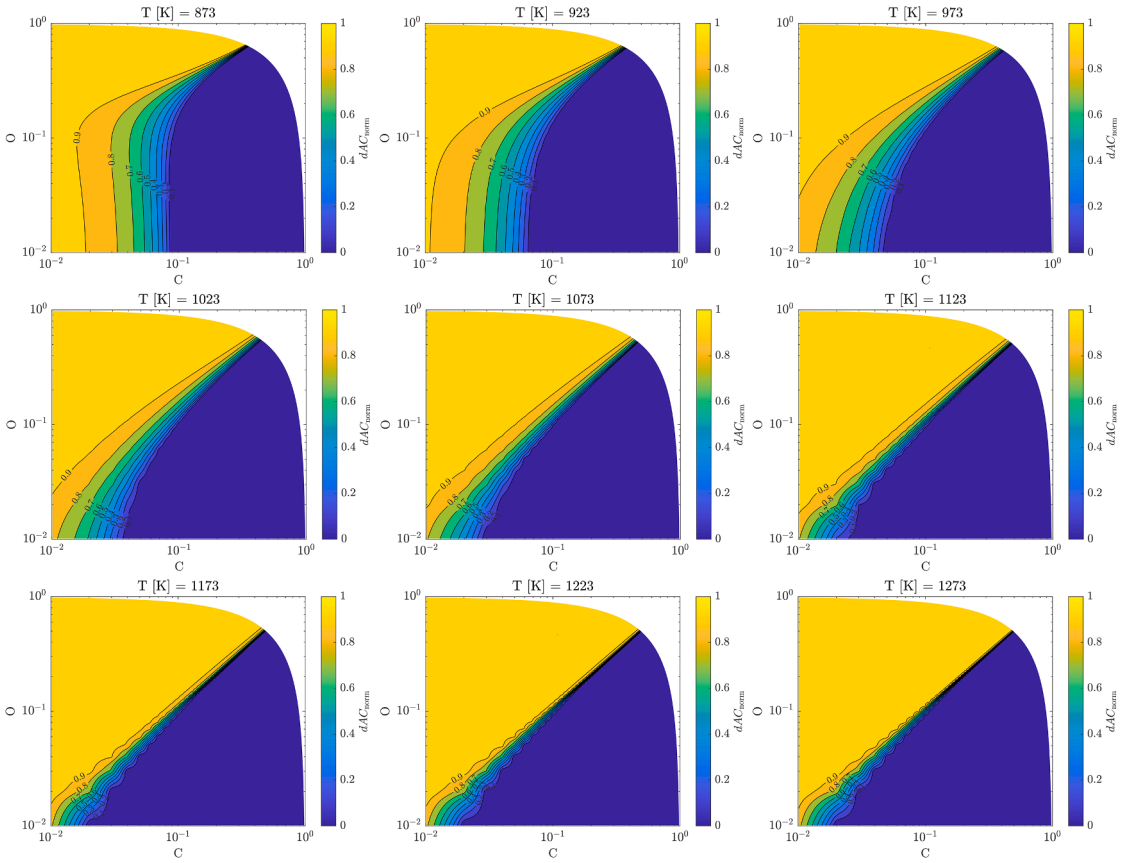

Figure 5. Two-dimensional iso-dAC_{norm}-C-O maps for temperatures from 873K to 1,273K at constant p = 1 bar
Contour undulations due to natural interpolation across more than 4,800 discrete C-H-O compositions per temperature step are shown.

on catalyst material and morphology, reactor and system, and local fluid conditions).

For the SOFC performance assessment, as the literature data on the cell performance were not reproducible due to the partial information on the SOFCs used and operating conditions, the presented iso-U_N maps and resulting recommendations in this work are based on the most common SOFC system, namely the methane-fueled, planar anode-supported IT-SOFC. Further, only H_2 conversion is considered for U_N here, although in reality both CH_4 and CO can be electrochemically converted in SOFCs. Including more competing reaction pathways could therefore further enhance model accuracy. Gas-phase transport diffusion and charge-transfer rates are also expected to affect the SOFC performance, but are not reflected in U_N.[54] Based on this, additional detailed assessments of AOG recirculation effects on the SOFC performance are thus recommended, in particular for other cell types (e.g., cathode supported or electrolyte supported) and cell configurations (e.g., tubular), fuels, and operating conditions.

The results from the literature cases as well as the presented 2D iso-dAC_{norm} and iso-U_N map indicate that, for a wide range of operating conditions, AOG recirculation mitigates the C-deposition risk while penalizing the SOFC performance. However, this trade-off is less pronounced under certain circumstances, such as for low C and O contents (e.g., by CO_2 removal before recirculation) or if the penalty on the Nernst potential from AOG recirculation is counteracted by a decreasing overpotential from activation, ohmic, or diffusion losses.[26]

Overall, with the introduction of the normalized carbon activity dAC_{norm}, the C-deposition risk becomes quantifiable and thus allows for a generalized assessment of safety margins independent of the system and use case as well as a more meaningful comparison between different SOFC designs with and without AOG recirculation under constant C-deposition risk and FU_{sys}.

Based on the proposed methodology, risk assessment maps, and presented results, we can thus conclude the following.

(1) The investigated literature cases based on conventional C-deposition risk assessment methods show largely varying conservative safety limits regarding C deposition. Hence, there is room to extend the envelope for safe operation of SOFC systems to achieve higher outputs.
(2) For all investigated literature cases (CH_4-fueled SOFC systems), AOG recirculation mitigates the C-deposition risk but is detrimental to the SOFC performance due to fuel dilution from the reaction products CO_2 and H_2O.
(3) For AOG recirculation to have little to no impact on the SOFC performance, the SOFC should be operated at

low C and O contents (e.g., ideally by CO_2 removal before recirculation), or the SOFC should be designed such that the penalty on the Nernst potential is compensated for with lower overpotentials or voltage drops to maintain the cell voltage output.

(4) To assess whether implementing AOG recirculation is beneficial on the stack, SOFC systems with AOG recirculation should be compared with single-pass SOFC systems at constant FU_{sys} and dAC_{norm} with the help of the provided maps. With this basis of comparison, the results indicate that, for C-deposition risk mitigation in CH_4-fueled, planar anode-supported SOFC stacks, increasing the fuel *SCR* is preferred to the recirculation of AOG.

(5) The presented maps for C-formation risk quantification are applicable to all chemical systems sensitive to C deposits working with hydrocarbons, such as the co-electrolysis of H_2O and CO_2.[55,56]

Since the current C-deposition risk assessment takes into account only solid graphite, future improvements could involve the extension of the current database in OpenCalphad with experimentally determined or modeled molar Gibbs energies of the different carbon allotropes (e.g., thermodynamics of the transformation of graphite to carbon nanotubes and vice versa,[52,57] of carbon nanotube formation with Ni catalysts,[58] of multi-walled carbon nanotubes,[59] or of carbon allotrope formation during catalytic reforming[47,60]). Finally, the developed model could be integrated into process optimization workflows to obtain high-performance SOFC system designs with extended stack operating windows that still comply with safety requirements.

METHODS

In this work, a new methodology is proposed for systematic and generalized assessments of the risks of C deposition for system, stack, and cell design and operation. The starting point is the introduction of the chemical activity as a quantity to quantify the C-deposition risk, which is then discussed within the framework of the open-source computational thermodynamics software OpenCalphad. The approach is then coupled with the existing solid oxide cell (SOC) model presented in Nakajo et al.[61,62] to investigate the details of the effect of AOG recirculation on the C-deposition risk and cell performance within a range of selected operating conditions studied in the literature. Using this quantitative C-deposition risk assessment method, general guidelines for AOG recirculation in SOFC systems are proposed.

The definition of activity

By convention, the activity a_i of a species i is dimensionless and defined as

$$a_i := \frac{f_i}{f^*} \quad (real) \qquad a_i := \frac{p_i}{p^*} \quad (ideal) \qquad \text{(Equation 1)}$$

with f^* being the fugacity for real gases and p^* the pressure for ideal gases in the standard state (typically $T^* = 298.15K$ and $p^* = 1$ bar). Thus, the notion of activity and its numerical value cannot be dissociated from the standard state. Following Equation 1, pure incompressible solids and liquids have an activity of unity. Note that a species is defined as a molecular-like aggregate of atoms or elements with fixed stoichiometry, such as H_2O.[63] The usage of species is the usual way of representing a phase in literature. However, it is also possible to describe a phase through its elementary components, as done in OpenCalphad.

The activity is endowed with the meaning of a change in chemical potential related to the evolution of a process away from the standard state as follows:

$$a_i = \exp\left(\frac{\mu_i - \mu_i^*}{RT}\right), \qquad \text{(Equation 2)}$$

with μ_i being the chemical potential of a constituent i in a gas phase, R the gas constant, and T the temperature.

The chemical potential μ_i of a species i describes its tendency to leave its current thermodynamic state physically, chemically, or biochemically.[64] It is defined as the molar partial Gibbs energy of a system at equilibrium:

$$\mu_i = \left.\frac{\partial G}{\partial N_i}\right|_{T,N_{j\neq i}}, \qquad \text{(Equation 3)}$$

with G being the Gibbs energy and N_i the molar amount of species i in the system.

The Gibbs energy was introduced as a criterion of equilibrium and to quantify the spontaneous evolution of thermodynamic processes at constant pressure and temperature.[65] It is defined as

$$\begin{aligned} G &:= U + pV - TS \\ &= H - TS \\ &= f(T, p, N_i) \end{aligned}, \qquad \text{(Equation 4)}$$

with the thermodynamic system's internal energy U (J), volume V (m^3), pressure p (Pa), temperature T (K), entropy S (kJ/kg K), and enthalpy H (kJ/kg). In a multi-species system, the Gibbs energy is therefore a function of temperature, pressure, and the molar amounts N_i (mol) of each species i in the system.

For an isothermal and isobaric thermodynamic system with a constant amount of all species, the equilibrium is reached when its Gibbs energy is at its minimum value and its change is zero:

$$dG = 0 \quad (equilibrium). \qquad \text{(Equation 5)}$$

The equilibrium of a system is thus found by minimizing dG, which—applying Equation 3—is defined as

$$\begin{aligned} dG &= V \cdot dp - S \cdot dT + \sum_i \left(\frac{\partial G}{\partial N_i} \cdot dN_i\right) \\ &= V \cdot dp - S \cdot dT + \sum_i (\mu_i \cdot dN_i) \end{aligned}, \qquad \text{(Equation 6)}$$

with $\frac{\partial G}{\partial N_i}$ being the partial derivative of the Gibbs energy with respect to the molar amount N_i of species i and μ_i being the chemical potential of species i in the system. Equation 5 and Equation 6, along with the measurement of temperature, pressure, and composition, enable the determination of the Gibbs energy of a system containing different species i at equilibrium.

Based on Equations 2, 3, 4, 5, and 6, the activity a_i is hence an experimentally measurable quantity for any non-charged compound (see Miki et al.[44] and Fruehan[45]) and depends on any

Please cite this article in press as: He et al., Chemical activity-based carbon-deposition risk maps for solid oxide fuel cell systems with off-gas recirculation, Cell Reports Physical Science (2026), https://doi.org/10.1016/j.xcrp.2026.103106

factor that affects the Gibbs energy, i.e., temperature, pressure, concentration, or intramolecular interactions. Since C deposition in SOFC systems comes in fact from a phase change of the gaseous fuel to form solid carbon, the C-deposition risk can thus be captured and quantified over the notion of activity.

Computational thermodynamics model

CALPHAD method

The CALPHAD method was originally developed for semi-empirical calculations of phase equilibria in alloys.[66,67] It is, however, suitable for determining the phase equilibria of many other substances as well as other phase-based material properties using models for describing the underlying physics (e.g., diffusion effects,[68] surface tension effects,[69] or thermal expansion[70]).

Phase equilibria are calculated by minimization of the Gibbs energy of the system under user-specified conditions, using techniques like the Lagrangian multiplier method,[71] grid minimization,[72] or a combination of both.[63] The parameters of the different models used to describe the Gibbs energy of individual phases are fitted to experimental and computational data from existing thermodynamic databases (TDBs) for binary and ternary systems, such as the commercial 1991 SGTE (Scientific Group Thermodata Europe) database for pure elements and substances[73] or the 1999 TCRAS (ThermoCenter of the Russian Academy of Science, IVTANTHERMO) database.[74] In doing so, the CALPHAD method allows the extrapolation from available data on binary and ternary systems into higher order systems, for which the information is difficult to obtain experimentally or not reported in the existing literature. Kattner[75] reviewed the CALPHAD method from the standpoint of the required models, data, and criteria for data quality assessment.

Numerical procedure of OpenCalphad

OpenCalphad describes a system of phases through its components E, which is an alternative to using species or constituents i as introduced previously. A constituent i is a species constituting a phase, while a component E is defined as an irreducible subset of a species, usually an element (e.g., a gas phase consisting of the constituents H_2O, H_2, and O_2 would thus have H and O as components). This allows the representation of different phase compositions and properties over a mixture of components, e.g., in C-H-O ternary-phase diagrams. Therefore, the following description distinguishes between constituents i and components or elements E of a phase α.

OpenCalphad uses the molar Gibbs energy based on the molar amount of formula units of a phase α, G_M^α (J/mol), so that

$$G = \sum_\alpha \left(\aleph^\alpha G_M^\alpha\right), \qquad \text{(Equation 7)}$$

with $\aleph^\alpha$ being the number of moles of formula units of the phase α in moles. Note that a formula unit is generally defined as the smallest set of ions to fully describe an ionic lattice or compound.

The Gibbs energy per mole of formula unit of a phase α is

$$G_M^\alpha = \sum_i \left(y_{i,s}^\alpha \cdot G_{M,i}^\alpha\right), \qquad \text{(Equation 8)}$$

with $G_{M,i}^\alpha$ being the molar Gibbs function of the constituent i per mole of formula unit of phase α and $y_{i,s}^\alpha$ being the fraction of constituent i in sublattice s of the phase α.

OpenCalphad takes $G_{M,i}^\alpha$ (J/mol) from databases such as IVTANTHERMO[76] or SGTE[73]: the general form for a gaseous constituent i in an ideal gas phase α is

$$G_{M,i}^\alpha = k_0 + k_1 T + k_2 T \cdot \ln(T) + k_3 T^2 + k_4 T^3 + k_5 T^{-1} + + R \cdot T \cdot \ln\left(\frac{p}{p^*}\right), \qquad \text{(Equation 9)}$$

with k_n being the parameters determined by fitting experimental data, T and p the temperature and pressure of the system, and p^* the pressure at standard conditions, here set to 1 bar. For a solid species i, the last term at the right-hand side in Equation 9 equates to zero. These correlations are valid for specific temperature ranges and hence have to be updated accordingly during iterative calculations.

The constituent fraction $y_{i,s}^\alpha$ is used as there may be more constituents than components in a phase, leading to internal degrees of freedom within the phase, which have to be taken into account during the equilibrium calculations.[77]

The sum of the fractions of constituents i on sublattice s in the phase α, $y_{i,s}^\alpha$, has to be unity:

$$\sum_i y_{i,s}^\alpha = 1. \qquad \text{(Equation 10)}$$

The number of moles of a component or element E per formula unit of a phase α is then provided by

$$M_E^\alpha = \sum_s n_s^\alpha \cdot \sum_i \left(b_{E,i} \cdot y_{i,s}^\alpha\right), \qquad \text{(Equation 11)}$$

with n_s^α being the number of sites for a sublattice s in the α phase and $b_{E,i}$ being the stoichiometric coefficient of element E in constituent i. For example, the stoichiometric coefficient of element H in constituent H_2O is $b_{H,H_2O} = 2$.

Note that the notion of sublattice is used to distinguish different tendencies of ionization of the constituents and thus plays a role only for phases that consist of several sublattice structures with different constituents. Gas phases have only one sublattice, while for the graphite phase, all sublattices have the same structure and contain pure C only.[78]

The molar fraction of component E in phase α is then

$$x_E^\alpha = \frac{M_E^\alpha}{M^\alpha}, \qquad \text{(Equation 12)}$$

with M^α being the total number of moles of all components in the α phase.

The total number of moles of an element E over all the phases of a system, N_E (which is usually known), is then

$$N_E = \sum_\alpha \aleph^\alpha M_E^\alpha. \qquad \text{(Equation 13)}$$

Lagrangian multiplier method

To determine the chemical potential μ_E and thus the activity a_E of a component E in the system at equilibrium at given conditions, the system's Gibbs energy has to be minimized following Equation 5. To do so numerically, the Lagrangian multiplier method is applied to Equation 7 with specified constraints and conditions.[71]

Equations 10 and 13 form the main constraints; another constraint is that the molar amount of metastable phases ϕ has to equal zero, as only stable phases exist at equilibrium:

$$\aleph^{\phi} = 0. \quad \text{(Equation 14)}$$

The Lagrange function L for the conditions of constant composition, temperature, and pressure is then

$$L = \sum_{\alpha} \aleph^{\alpha} G_M^{\alpha}\left(T, p, y_{i,s}^{\alpha}\right) + \sum_{E} \mu_E \left(\sum_{\alpha} \aleph^{\alpha} M_E^{\alpha} - N_E\right) + \sum_{\alpha}\sum_{s} \eta_s^{\alpha}\left(1 - \sum_{i} y_{i,s}^{\alpha}\right) + \sum_{\phi} \gamma^{\phi} \aleph^{\phi}, \quad \text{(Equation 15)}$$

where α denotes all the stable phases and ϕ denotes all metastable phases, with subscripts for element E and sublattice s of a constituent i in the system. μ_E, η_s^{α}, and γ^{ϕ} are the Lagrangian multipliers. More constraints and thus Lagrangian multipliers can be added, e.g., if the pressure p is not set constant.

The Lagrange function has the same minimum as the Gibbs energy function if all constraints are active, so the equilibrium criterion Equation 5 is valid on L. Further, Hillert, in 1981,[71] highlighted that the partial derivation of L with respect to the amount of each stable phase α at its minimum reveals that the Lagrange multiplier μ_E is identical to the chemical potential of the component E in the system (similar to Equation 3),

$$\begin{aligned} \frac{\partial L}{\partial \aleph^{\alpha}} &= G_M^{\alpha} - \sum_{E} M_E^{\alpha} \cdot \mu_E = 0 \\ G_M^{\alpha} &= \sum_{E} \left(M_E^{\alpha} \cdot \mu_E\right) \end{aligned}. \quad \text{(Equation 16)}$$

The equilibrium is found by solving the Lagrange function (Equation 15) using linear iterative methods (e.g., the Newton-Raphson technique), starting with an initial estimate for the stable phases α and their constitution for the given conditions. OpenCalphad uses a grid minimizer for the first estimation of the stable phases. As described in Chen,[72] the Gibbs energy of each phase is approximated and the set of phases and constitutions with the lowest Gibbs energy for the given conditions are selected. $\aleph^{\alpha}$, $y_{i,s}^{\alpha}$, μ_E, and γ^{ϕ} are then determined from the initial guess by solving Equation 15 iteratively along with updates of the constraints until convergence is reached. As an example for constraint updating, for the calculation of the set of stable phases, detected metastable phases are removed from the calculation ($\aleph^{\alpha} < 0$ or $\gamma^{\phi} > 0$).

The algorithm for the calculation of a single and global equilibrium is detailed by Sundman et al.[63,79]

C-deposition risk assessment using OpenCalphad

Based on the above-mentioned numerical procedure, OpenCalphad calculates the activity a_E from the chemical potential at equilibrium μ_E based on Equation 2 assuming ideal gas behavior. For a given composition, temperature, pressure, and total amount of components, the activity can thus be determined for all the components E of the system. Since SOFCs consume and convert hydrocarbon fuels, C, H, and O are the main components in the system, and the existing thermodynamic database for C, H, and O components is applied here (*CHO-gas.TDB* from OpenCalphad, based on Dinsdale[73] and Belov et al.[74]) for the calculation of the chemical activity.

In a ternary system at equilibrium containing the components C, H, and O, the activity of component C, a_C, equals the activity of graphite, a_C^{graphite}, when there is C deposition. This is illustrated by an *ad hoc* OpenCalphad calculation for a system consisting of 12 mol C, 15 mol O, and 73 mol H at 1 bar in Figure S4: the solid carbon phase (red curve in Figure S4B) is stable ($x^{\text{graphite}} > 0$) in the temperature ranges between 300K–413K and 719K–958K, which corresponds to ranges where the activity profile of the example C-H-O system (a_C) matches the activity of a system consisting of 100% C in the form of graphite $\left(a_C^{\text{graphite}}\right)$.

Therefore, in this work, the condition for C formation is defined as the point at which the activity difference dAC between the C components of the fuel a_C and of pure graphite a_C^{graphite} equals zero:

$$dAC := a_C - a_C^{\text{graphite}} = 0. \quad \text{(Equation 17)}$$

When a fuel has no C components, the C-deposition risk is naturally at its minimum, leading to the activity difference dAC_{noC}, which is defined as follows:

$$dAC_{\text{noC}} := a_C(\text{noC}) - a_C^{\text{graphite}} = 0 - a_C^{\text{graphite}}, \quad \text{(Equation 18)}$$

with a_C(noC) being the activity of the species C in a system where the amount of C is minimal, which equals zero if no C exists. Thus, at zero C-deposition risk at a given temperature T, the activity difference between the fuel and the graphite is the negative of the activity of pure graphite: $dAC = dAC_{\text{noC}} = -a_C^{\text{graphite}}$.

Since the numerical value of activity or dAC depends highly on the chosen standard condition, the C-deposition risk—or, in conventional terms, the "distance" of an operating point relative to the C-formation boundary ($dAC = 0$)—can be quantified at a given temperature T by normalizing the activity difference between the fuel and the graphite dAC, with the activity difference at zero C-deposition risk dAC_{noC}. Hence, we introduce here the quantifiable C-deposition risk, dAC_{norm}, defined as

$$dAC_{\text{norm}} := \frac{dAC}{dAC_{\text{noC}}} = \frac{a_C - a_C^{\text{graphite}}}{-a_C^{\text{graphite}}}. \quad \text{(Equation 19)}$$

For the sake of completion, apart from the above-introduced C-deposition risk parameter dAC_{norm} (Equation 19), the conventional C-deposition risk assessment parameters SCR and OCR are mentioned in the following:

$$\begin{aligned} SCR &= \frac{y_{H_2O}}{y_{CH_4} + y_{CO} + y_{CO_2}} \\ OCR &= \frac{y_{H_2O} + y_{CO} + 2 \cdot y_{CO_2}}{y_{CH_4} + y_{CO} + y_{CO_2}} \end{aligned}, \quad \text{(Equation 20)}$$

with y_i being the molar fraction of the species i in the fuel at the inlet of the SOFC. In practice, stoichiometric SCR or OCR values are applied based on the inlet composition to prevent C formation, e.g., $SCR = OCR > 2$ for SMR.

Interface with continuum SOFC model

OpenCalphad calculations were interfaced with a continuum model of SOFC and stack with finite-difference discretization along the cell thickness and gas flow directions. The implementation allows for the automated screening of the trade-off between stack performance and risks of C deposition at each location in the discretization of the gas channel and anode substrate, during steady-state or dynamic operation conditions, with or without AOG recirculation.

The baseline SOFC stack model version used in the present study is modular and consists of a single repeating unit (SRU) in an assembly of metallic interconnects, gas channels, and cell submodels. The two first are discretized along the flow path to solve in-plane heat and mass transport with boundary conditions representative of the conditions of a stack in an insulation in co- or counter-flow configurations. Each grid point along the flow path is coupled to 1D discretizations through the thickness of the cell to solve gas, ions, and electron transport and transfer. The dusty-gas model[80,81] is used for the simulation of multi-component gas-phase transport in the porous electrodes, substrates, and contact layers. It is coupled with heterogeneous catalytic reactions and distributed charge transport and transfer, with reaction pathways on the anode and cathode sides, depending upon operation regimes and materials (Ni-YSZ anode, LSM-YSZ, LSCF, or LSCF-GDC cathode). The material parameters used in the present study correspond to the Ni-YSZ anode, LSCF-GDC/LSCF cathode contract layer, and YSZ electrode with GDC interlayer characterized in Rinaldi et al.,[82] respectively. Considered species are H_2, H_2O, CH_4, CO, and CO_2 on the anode side and O_2 and N_2 on the cathode side. The anode model applies the standard assumption in SOFC modeling that only H_2 is electrochemically converted at triple-phase boundaries. It therefore assumes that CH_4 and CO are consumed by SMR and the water-gas shift (WGS) reactions near equilibrium at all locations within the Ni-YSZ anode. The governing equations of the SOFC model for the physics and reaction pathways relevant for the IT anode-supported technology are implemented in an equation-oriented process modeling tool (gPROMS). Detailed descriptions of their implementation and model calibration on experimental current-voltage characteristics and distribution of relaxation times (DRT) are available in Caliandro et al.[83]

The main SOFC parameters of interest in this study are the fuel utilization ratio *FU* of the SOFC, generally defined as the ratio of reacted fuel over the fuel input:

$$FU = \frac{\dot{N}_{\text{fuel,in}} - \dot{N}_{\text{fuel,out}}}{\dot{N}_{\text{fuel,in}}} = \frac{\dot{N}_{\text{fuel,reacted}}}{\dot{N}_{\text{fuel,in}}}, \qquad \text{(Equation 21)}$$

with $\dot{N}$ being the molar flow (mol/s) of the fuel at the inlet and outlet sections of the SOFC. Depending on the boundary (which can differ based on whether AOG is recirculated or not, see Figure 6), the system fuel utilization FU_{sys} and local fuel utilization FU_{loc} can be defined as follows:

$$\begin{aligned} FU_{\text{sys}} &= \frac{\dot{N}_{\text{fuel,1}} - \dot{N}_{\text{fuel,4}}}{\dot{N}_{\text{fuel,1}}} \\ FU_{\text{loc}} &= \frac{\dot{N}_{\text{fuel,2}} - \dot{N}_{\text{fuel,3}}}{\dot{N}_{\text{fuel,2}}} \end{aligned}, \qquad \text{(Equation 22)}$$

with $\dot{N}_n$ being the molar flow (mol/s) of the fuel at section *n* of the system (n = 1,4, inlet and outlet boundary of the SOFC system, including AOG recirculation; n = 2,3, inlet and outlet boundary of the SOFC stack). It becomes clear that, for a single-pass system without AOG recirculation, $FU_{\text{sys}} = FU_{\text{loc}}$. In a system with AOG recirculation, the *RR* relates to the system and local fuel utilization ratios as follows:

$$RR = \frac{FU_{\text{sys}} - FU_{\text{loc}}}{FU_{\text{sys}} \cdot (1 - FU_{\text{loc}})}. \qquad \text{(Equation 23)}$$

For the present study, the control of the AOG *RR* is implemented in the SOFC model in the form of user-specified fractions of recirculated off-gas species mass flows, assuming no pressure losses in the stack and that the recirculated AOG is of the same pressure as at the anode inlet, $p_{\text{AOGR}} = p_{in}$.

As previously stated, since only H_2 is assumed to be electrochemically converted in the SOFC model (CH_4 and CO fluxes toward the anode consumed via SMR and WGS reactions), the cell performance is assessed over the Nernst potential U_N (V) based on the gas composition at the anode inlet based on H_2 oxidation ($H_2 + 0.5O_2 \rightleftharpoons H_2O$):

$$\begin{aligned} U_N &= U^*_{\text{rev}} - \frac{1}{z_e \cdot F} \cdot RT \ln\left(\frac{\Pi_{\text{prod},k} a_k^{y_k}}{\Pi_{\text{react},j} a_j^{y_j}}\right) \\ &= \frac{1}{z_e \cdot F} \cdot \left[-\Delta G^* - RT \ln\left(\frac{\Pi_{\text{prod},k} a_k^{y_k}}{\Pi_{\text{react},j} a_j^{y_j}}\right)\right] \quad (real), \\ &= \frac{1}{2 \cdot F} \cdot \left[-\Delta G^* - RT \ln\left(\frac{p_{H_2O}}{p_{H_2} \cdot p_{O_2}^{0.5}}\right)\right] \quad (ideal) \end{aligned} \qquad \text{(Equation 24)}$$

with U^*_{rev} (V) being the reversible potential of the reaction at standard state (25°C, 1 atm) (for H_2 oxidation: U^*_{rev,H_2} = 1.229 V), ΔG^* (J) the Gibbs free reaction energy at standard state (for H_2 oxidation: 237.1 kJ/mol), *R* (J/molK) the universal gas constant, z_e the number of electrons exchanged within the reaction (for H_2 oxidation: z_e = 2), *F* (C/mol) the Faraday constant, *T* (K) the temperature, $a_{j,k}$ the activity of reactant *j* or product *k*, y_i the molar fraction of a species *i*, and p_i (Pa) the partial pressure of species *i*.

Other relevant SOFC parameters are the average current density j_{avg} (A cm^{-2}), inlet and outlet temperatures T_{in} (K) and $T_{\text{PEN, max}}$ (K) (maximum temperature located at the outlet), and the inlet and operating pressures $p_{\text{in}} = p_{\text{SOFC}}$ = 1 atm of the stack. Further, dry air (21% O_2, 79% N_2) has been assumed at the cathode side.

For the combined assessment of C-deposition risk and SOFC performance, the OpenCalphad-gPROMS interface implemented in MATLAB executes automatically and sequentially the following tasks: (1) user-specified range of operation conditions as input; (2) batch run of the SOFC model; (3) post-processing of anode-side gas compositions, pressure, and temperature, along with cell or stack performance metrics; (4) OpenCalphad batch runs for each local condition in the anode channel compartment and Ni-YSZ electrode computed by the SOFC model in (2); and (5) post-processing of OpenCalphad simulation results (see Figure 7). For the visual display of the simulation

Cell Reports
Physical Science
Article

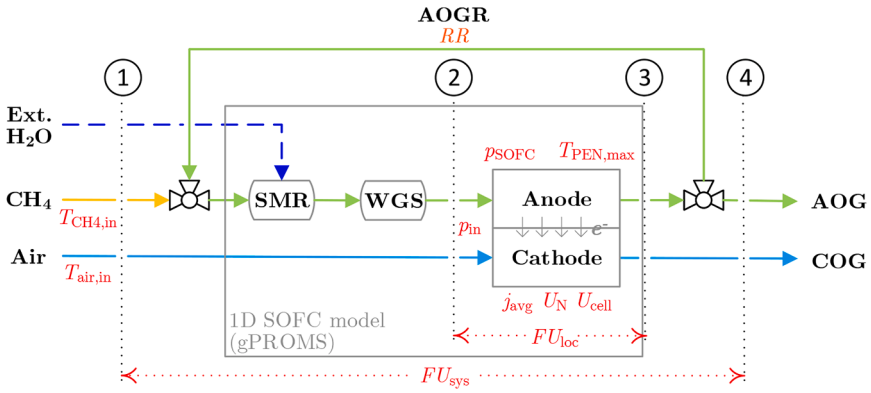

Figure 6. SOFC system with AOG recirculation as modeled in the gPROMS SOFC model

SMR and WGS reactions before anode-side reaction (H_2 oxidation), assuming no pressure losses in the stack with $p_{AOGR} = p_{in}$. Numbered main sections and key parameters are in red. The dashed line for the external H_2O input indicates that its required amount depends on the amount of recirculated H_2O.

results in a C-H-O ternary diagram, an open-source MATLAB package[84] has been modified and applied.

Model assumptions and limitations

The main assumptions and limitations of the developed coupled SOFC-OpenCalphad modeling approach are as follows.

(1) The C-formation risk is determined at thermodynamic equilibrium, considering graphitic carbon only. No reaction kinetics, catalyst morphology influences, or resulting formation of other carbon allotropes such as carbon whiskers[15,16,18] were considered here, since these effects are highly case specific and currently not well understood.

(2) The chemical activity as an indicator for C deposition is limited to ternary (C, H, and O) and higher-order component systems in OpenCalphad. For unitary or binary component systems (C and H or C and O), the system of equations to solve for the chemical activity is underdetermined; hence, for these cases, the Gibbs energy of the graphite phase is a better measure, i.e., $G_C = 0$ is the necessary condition for C deposition.

(3) The model results are subjected to the underlying thermodynamic database and database accuracy. Here, the standard C-H-O thermodynamic database in OpenCalphad, which is based on established, commercial databases by SGTE[73] and TCRAS, is used.[74] Therefore, the anticipated database discrepancies are negligible, especially since the C-H-O system has been extensively studied in literature and is considered classical.

(4) The current gPROMS SOFC model has been experimentally validated and calibrated for the anode-supported planar SOFCs. Therefore, all cell performance assessments and resulting recommendations presented here are based on this SOFC type.

(5) The standard assumption of only H_2 being electrochemically converted at triple-phase boundaries is applied here, owing to its significantly higher reaction rate compared with the competing CO and CH_4 oxidation pathways,[85] following the set of elementary processes proposed and experimentally validated by Zhu et al.[86]

These assumptions and limitations do not compromise results validity, as the aim here is to propose a risk assessment framework with high generalizability for the practical safety margin quantification in C-H-O ternary systems independent of system-specific configurations or use case. Overcoming these limitations represents the next step in the level of detail.

Model validation with literature cases

Four literature cases were selected to validate the developed coupled SOFC-OpenCalphad modeling approach to ensure generalizability of the results. The cases include combined experimental and numerical investigations of the C-deposition risk in the form of graphite for different IT-SOFC systems and cell types during operation with and without AOG recirculation, using conventional C-deposition risk assessment methods (see Table 1).

The operating conditions from the literature cases are applied in the SOFC-OpenCalphad model for comparison of the results and validation of the model. Not all information that is required as an input for the SOFC-OpenCalphad model—such as the operating conditions of the SOFC (T_{in}, $T_{PEN,max}$,j_{avg}, etc.)—could be found in the selected literature. However, the missing data were inferred through inverse modeling, i.e., by iteratively adjusting them until the model outputs reproduced the published results, validating the established model in the process. The inferred parameters were subsequently evaluated for physical plausibility and have been verified to be consistent with established engineering principles and comparable studies. Table 2 summarizes the operating conditions of the investigated literature cases used in the SOFC-OpenCalphad model to replicate the literature data.

Case 1

Henke et al.[22] investigated the effect of AOG recirculation on C formation in a planar IT-SOFC under different operating conditions and fuels. The software package Cantera was used to calculate the thermodynamic equilibrium (via Gibbs energy minimization) and thus to determine the C-deposition boundary for graphite, or more specifically, the C-formation temperatures for different *RR* and FU_{loc} for natural gas and biogas as fuels. However, they did not mention the SOFC operating conditions nor the anode inlet fuel composition for different *RR* and *FU*, nor was information on the amount of external H_2O used or on the re-former given. Hence, the SOFC operating conditions such as inlet fuel and air temperatures or current density were obtained by replicating the operating point given for natural

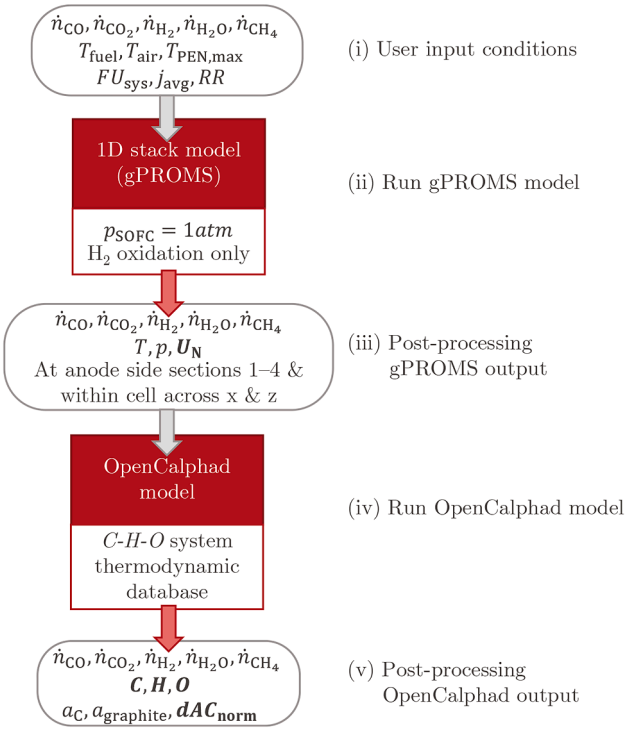

Figure 7. Simulation procedure of the OpenCalphad-SOFC model for calculating C-deposition risk and SOFC performance

Locations of sections 1–4 depicted in Figure 6.

gas (see Table 2 of Henke et al.[22]), leading to a well-matching anode inlet gas composition (C-H-O = 0.131-0.522-0.347, error $\leq$0.42%). The comparison between their results and the present model is presented in Figure 8A as a function of FU_{loc}, showing a high level of agreement of the obtained results with the literature data for the C-formation temperatures (maximum error of 3.3%).

Case 2

Liu et al.[25] applied methods similar to those in case 1 to a 5-kW tubular cathode-supported IT-SOFC stack with an ejector-driven AOG recirculation. They simulated the effects of fuels (syngas and natural gas) and ejector inlet pressure on *RR*, stack current, and cell voltage, as well as the C-formation risk using Factsage. Instead of the C-formation temperature, Liu et al.[25] used the *OCR* as an indicator for C-deposition-free operation. With the SOFC-OpenCalphad model, the recalculation of the *OCR* at constant FU_{sys} of 0.8, an inlet temperature of 1,183K, and a varying average current density j_{avg} (as in Figure 8 of Liu et al.[25]) using CH_4 as fuel shows very good agreement with the literature data, especially for *RR* up to 0.685 (see Figure 8B). The agreement decreases slightly when reaching ejector criticality (maximum error of 4.88%). It also becomes clear that, with increasing *RR*, the *OCR* of the fuel at the SOFC inlet increases as well.

Case 3

Terayama et al.[26] investigated experimentally the operation of a CH_4-fed planar anode-supported single-cell IT-SOFC system under single-pass and AOG recirculation conditions. However, due to the complexity and low availability of high-temperature AOG recycle blowers, they did not carry out real AOG recirculation tests but instead used AOG compositions obtained with externally supplied and catalytically converted H_2, O_2, and CO_2 to mimic AOG recirculation conditions. As a consequence, the indicated *FU* for the AOG recirculation conditions are both local and system fuel utilization ratios (see Equation 22). Thus, in the following, only the term FU_{sys} is used. The C-deposition risk was analyzed at the inlet of the pre-re-former—where the simulated AOG is injected at a temperature lower than the stack—and determined over the C formation temperature using the process simulation software HSC Chemistry. Terayama et al.[26] determined safe operating conditions for *RR* from 0.4 to 0.8 and different FU_{sys}. For the same operating conditions, the C-formation temperatures obtained from the SOFC-OpenCalphad model show very high agreement (maximum error of 0.994%) (see Figure 8C).

Case 4

Baba et al.[23,24] experimentally investigated a 1-kW tubular CH_4-fed IT-SOFC stack under full-load (3.15 L/min CH_4 flow rate) and part-load operation (CH_4 flow rates from 1.96 to 2.51 L/min) under constant FU_{sys} of 0.84. Steam for the re-forming of CH_4 was not supplied externally but provided by AOG recirculation via ejector-driven recirculation. The C-deposition risk was evaluated using a fixed *OCR* threshold of 2[23] and, further, in a binary way over the C-formation boundary in classical C-H-O ternary diagrams.[24] Using the same experimental conditions, recalculating the C-H-O ternary diagram for the gas composition at the stack inlet with the SOFC-OpenCalphad model yields similar results (maximum error of 7%) (see Figure 8D).

In light of the high level of agreement between the obtained results compared to the published data based on the conventional C-deposition risk assessment methods (*OCR*, T_{Cdep}, and C-H-O ternary diagram) within the anticipated database discrepancies, the proposed SOFC-OpenCalphad model is considered validated.

RESOURCE AVAILABILITY

Lead contact

Requests for further information and resources should be directed to and will be fulfilled by the lead contact, Victoria He (victoria.he@epfl.ch).

Materials availability

This study did not generate new materials.

Data and code availability

- All data reported in this paper will be shared by the lead contact upon request.
- This paper does not report original code.
- Any additional information required to reanalyze the data reported in this paper is available from the lead contact upon request.

ACKNOWLEDGMENTS

This work was funded by the European Union's Horizon 2020 Research and Innovation Program via grant award no. 815284, funder ID: https://doi.org/10.13039/501100000780.

AUTHOR CONTRIBUTIONS

V.H.: conceptualization, methodology, formal analysis, data curation, and writing – original draft. A.N.: methodology, formal analysis, data curation,

Cell Reports
Physical Science
Article

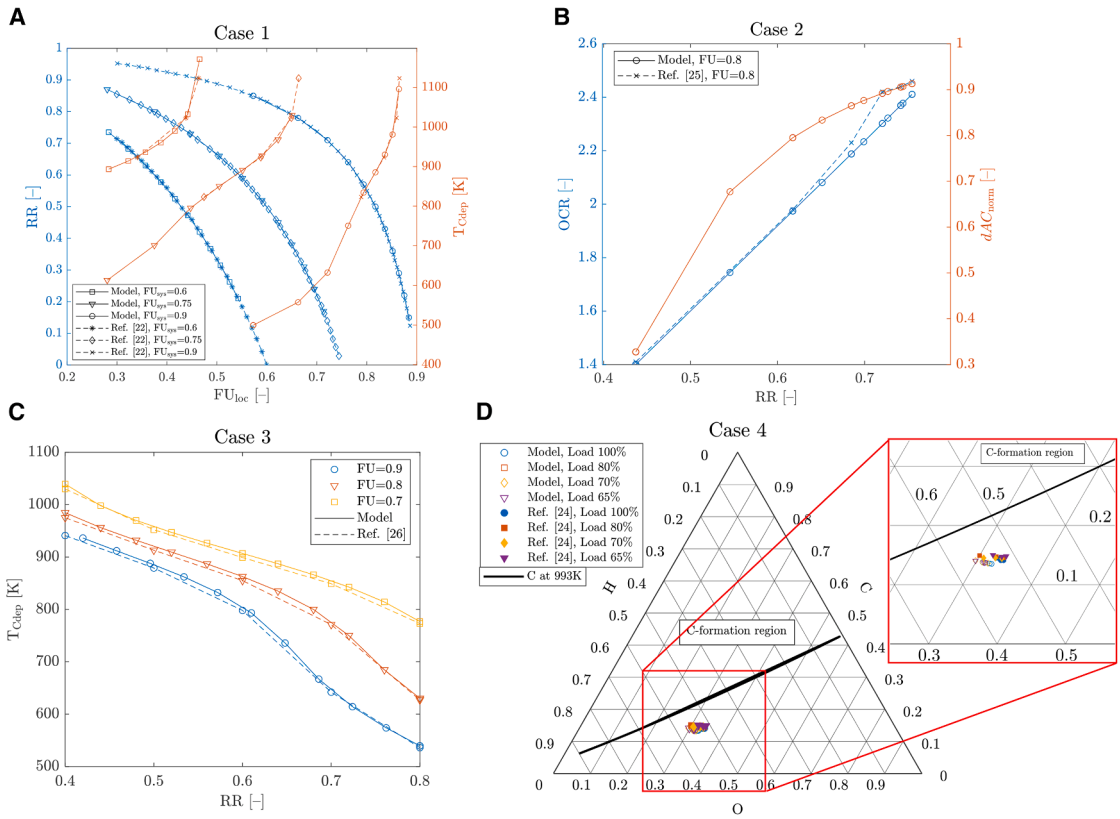

Figure 8. Validation of the SOFC-OpenCalphad model with literature cases 1–4 via replication of literature plots with conditions based on Table 2

(A) C-deposition temperatures for different *RR* and *FU* of case 1 in comparison with Figure 2 of Henke et al.[22]

(B) *OCR* and dAC_{norm} over *RR* of case 2 in comparison with Figures 7 and 8 of Liu et al.[25]

(C) C-deposition temperature over *RR* of case 3 in comparison with Figure 4 of Terayama et al.[26]

(D) C-H-O ternary diagram for full- and part-load operation and *RR* of case 4 in comparison with Figure 4 of Baba et al.[24]

and writing – review & editing. M.P.-F.: conceptualization, methodology, and writing – review & editing. J.V.h.: writing – review & editing, funding acquisition. J.S.: writing – review & editing, funding acquisition, and supervision.

DECLARATION OF INTERESTS

The authors declare no competing interests.

SUPPLEMENTAL INFORMATION

Supplemental information can be found online at https://doi.org/10.1016/j.xcrp.2026.103106.

Received: June 24, 2025
Revised: November 19, 2025
Accepted: January 9, 2026

REFERENCES

1. Shi, H., Su, C., Ran, R., Cao, J., and Shao, Z. (2020). Electrolyte materials for intermediate-temperature solid oxide fuel cells. Prog. Nat. Sci. Mater. Int. *30*, 764–774. https://doi.org/10.1016/j.pnsc.2020.09.003.

2. Brett, D.J.L., Atkinson, A., Brandon, N.P., and Skinner, S.J. (2008). Intermediate temperature solid oxide fuel cells. Chem. Soc. Rev. *37*, 1568–1578. https://doi.org/10.1039/B612060C.

3. Tsai, T., and Barnett, S.A. (1997). Effect of LSM-YSZ cathode on thin-electrolyte solid oxide fuel cell performance. Solid State Ionics *93*, 207–217. https://doi.org/10.1016/S0167-2738(96)00524-3.

4. Nielsen, E.R., Prag, C.B., Bachmann, T.M., Carnicelli, F., Boyd, E., Walker, I., Ruf, L., and Stephens, A. (2019). Status on Demonstration of Fuel Cell Based Micro-CHP Units in Europe. Fuel Cells *19*, 340–345. https://doi.org/10.1002/fuce.201800189.

5. Liu, J., and Barnett, S.A. (2003). Operation of anode-supported solid oxide fuel cells on methane and natural gas. Solid State Ionics *158*, 11–16. https://doi.org/10.1016/S0167-2738(02)00769-5.

6. Subotic, V., Baldinelli, A., Barelli, L., Scharler, R., Pongratz, G., Hochenauer, C., and Anca-Couce, A. (2019). Applicability of the SOFC technology for coupling with biomass-gasifier systems: Short- and long-term experimental study on SOFC performance and degradation behaviour. Appl. Energy *256*, 113904. https://doi.org/10.1016/j.apenergy.2019.113904.

7. Gadsbøll, R.Ø., Thomsen, J., Bang-Møller, C., Ahrenfeldt, J., and Henriksen, U.B. (2017). Solid oxide fuel cells powered by biomass gasification for high efficiency power generation. Energy *131*, 198–206. https://doi.org/10.1016/j.energy.2017.05.044.

8. Gandiglio, M., Lanzini, A., Santarelli, M., Acri, M., Hakala, T., and Rautanen, M. (2020). Results from an industrial size biogas-fed SOFC plant

(the DEMOSOFC project). Int. J. Hydrogen Energy *45*, 5449–5464. https://doi.org/10.1016/j.ijhydene.2019.08.022.

9. Sengodan, S., Lan, R., Humphreys, J., Du, D., Xu, W., Wang, H., and Tao, S. (2018). Advances in reforming and partial oxidation of hydrocarbons for hydrogen production and fuel cell applications. Renew. Sustain. Energy Rev. *82*, 761–780. https://doi.org/10.1016/j.rser.2017.09.071.
10. Fang, Q., Blum, L., Peters, R., Peksen, M., Batfalsky, P., and Stolten, D. (2015). SOFC stack performance under high fuel utilization. Int. J. Hydrogen Energy *40*, 1128–1136. https://doi.org/10.1016/j.ijhydene.2014.11.094.
11. Ahmed, K. (1997). Internal Steam Reforming of Partially Pre-Reformed Natural Gas In SOFC Stacks. SAVE Proc. *1997–40*, 228–234. https://doi.org/10.1149/199740.0228PV.
12. Chen, T., Wang, W.G., Miao, H., Li, T., and Xu, C. (2011). Evaluation of carbon deposition behavior on the nickel/yttrium-stabilized zirconia anode-supported fuel cell fueled with simulated syngas. J. Power Sources *196*, 2461–2468. https://doi.org/10.1016/j.jpowsour.2010.11.095.
13. Gemmen, R.S., and Johnson, C.D. (2006). Evaluation of fuel cell system efficiency and degradation at development and during commercialization. J. Power Sources *159*, 646–655. https://doi.org/10.1016/j.jpowsour.2005.10.109.
14. Nakajo, A., Mueller, F., Brouwer, J., Van herle, J., and Favrat, D. (2012). Progressive activation of degradation processes in solid oxide fuel cells stacks: Part I: Lifetime extension by optimisation of the operating conditions. J. Power Sources *216*, 449–463. https://doi.org/10.1016/j.jpowsour.2012.05.078.
15. Rostrup-Nielsen, J., and Trimm, D.L. (1977). Mechanisms of carbon formation on nickel-containing catalysts. J. Catal. *48*, 155–165. https://doi.org/10.1016/0021-9517(77)90087-2.
16. Helveg, S., Sehested, J., and Rostrup-Nielsen, J.R. (2011). Whisker carbon in perspective. Catal. Today *178*, 42–46. https://doi.org/10.1016/j.cattod.2011.06.023.
17. Baker, R. (1972). Nucleation and growth of carbon deposits from the nickel catalyzed decomposition of acetylene. J. Catal. *26*, 51–62. https://doi.org/10.1016/0021-9517(72)90032-2.
18. Yang, R. (1989). Mechanism of carbon filament growth on metal catalysts. J. Catal. *115*, 52–64. https://doi.org/10.1016/0021-9517(89)90006-7.
19. Subotic, V., Harter, P., Kusnezoff, M.,W., Napporn, T., Schroettner, H., and Hochenauer, C. (2021). Identification of carbon deposition and its removal in solid oxide fuel cells by applying a non-conventional diagnostic tool. Sustain. Energy Fuels *5*, 2065–2076. https://doi.org/10.1039/D0SE01914C.
20. Lanzini, A., Leone, P., Guerra, C., Smeacetto, F., Brandon, N.P., and Santarelli, M. (2013). Durability of anode supported Solid Oxides Fuel Cells (SOFC) under direct dry-reforming of methane. Chem. Eng. J. *220*, 254–263. https://doi.org/10.1016/j.cej.2013.01.003.
21. Shi, N., Xie, Y., Yang, Y., Xue, S., Li, X., Zhu, K., Huan, D., Peng, R., Xia, C., and Lu, Y. (2020). Review of anodic reactions in hydrocarbon fueled solid oxide fuel cells and strategies to improve anode performance and stability. Mater. Renew. Sustain. Energy *9*, 6. https://doi.org/10.1007/s40243-020-0166-8.
22. Henke, M., Hillius, S., Riedel, M., Kallo, J., and Friedrich, K.A. (2016). Gas Recirculation at the Hydrogen Electrode of Solid Oxide Fuel Cell and Solid Oxide Electrolysis Cell Systems. Fuel Cells *16*, 584–590. https://doi.org/10.1002/fuce.201500114.
23. Baba, S., Takahashi, S., Kobayashi, N., and Hirano, S. (2015). Evaluation of solid oxide fuel cell performance with anode recirculation using variable flow ejector at rated conditions. Mechanical Engineering Journal *2*, 4. https://doi.org/10.1299/mej.15-00087.
24. Baba, S., Takahashi, S., Kobayashi, N., and Hirano, S. (2020). Performance of anodic recirculation by a variable flow ejector for a solid oxide fuel cell system under partial loads. Int. J. Hydrogen Energy *45*, 10039–10049. https://doi.org/10.1016/j.ijhydene.2020.01.191.
25. Liu, M., Lanzini, A., Halliop, W., Cobas, V.R.M., Verkooijen, A.H.M., and Aravind, P.V. (2013). Anode recirculation behavior of a solid oxide fuel cell system: A safety analysis and a performance optimization. Int. J. Hydrogen Energy *38*, 2868–2883. https://doi.org/10.1016/j.ijhydene.2012.12.070.
26. Terayama, T., Momma, A., Tanaka, Y., and Kato, T. (2016). Improvement of Single Solid Oxide Fuel Cell Performance by Using Anode Off-Gas Recycle. J. Electrochem. Soc. *163*, F1380–F1388. https://doi.org/10.1149/2.09001613jes.
27. Colpan, C.O. (2009). Thermal Modeling of Solid Oxide Fuel-Cell Based Biomass Gasification Systems (Text Carleton University).
28. Ma, S., Loreti, G., Wang, L., Maréchal, F., Van herle, J., and Dong, C. (2022). Comparison and optimization of different fuel processing options for biogas-fed solid-oxide fuel cell plants. Int. J. Hydrogen Energy *47*, 551–564. https://doi.org/10.1016/j.ijhydene.2021.10.025.
29. Pérez-Fortes, M., He, V., Nakajo, A., Schiffmann, J., Maréchal, F., and Van herle, J. (2021). Techno-Economic Optimization of an Integrated Biomass Waste Gasifier–Solid Oxide Fuel Cell Plant. Front. Energy Res. *9*, 665585. https://doi.org/10.3389/fenrg.2021.665585.
30. Schäfer, F., Egger, S., Steiner, D., Carré, M., and Eichel, R.A. (2022). Control of oxygen-to-carbon ratio and fuel utilization with regard to solid oxide fuel cell systems with anode exhaust gas recirculation: A review. J. Power Sources *524*, 231077. https://doi.org/10.1016/j.jpowsour.2022.231077.
31. Tanaka, Y., Momma, A., Sato, K., and Kato, T. (2011). Improvement of Electrical Efficiency of Solid Oxide Fuel Cells by Anode Gas Recycle. ECS Trans. *30*, 145–150. https://doi.org/10.1149/1.3562470.
32. Halinen, M., Thomann, O., and Kiviaho, J. (2012). Effect of Anode off-gas Recycling on Reforming of Natural Gas for Solid Oxide Fuel Cell Systems. Fuel Cells *12*, 754–760. https://doi.org/10.1002/fuce.201200047.
33. Mastropasqua, L., Campanari, S., and Brouwer, J. (2017). Solid Oxide Fuel Cell short stack performance testing - part B: Operation in carbon capture applications and degradation issues. J. Power Sources *371*, 238–248. https://doi.org/10.1016/j.jpowsour.2017.10.014.
34. Cairns, E.J., Tevebaugh, A.D., and Holm, G.J. (1963). Thermodynamics of Hydrocarbon Fuel Cells. J. Electrochem. Soc. *110*, 1025. https://doi.org/10.1149/1.2425577.
35. Sasaki, K., and Teraoka, Y. (2003). Equilibria in Fuel Cell Gases : II. The C-H-O Ternary Diagrams. J. Electrochem. Soc. *150*, A885. https://doi.org/10.1149/1.1577338.
36. Kuhn, J., and Kesler, O. (2015). Carbon deposition thresholds on nickel-based solid oxide fuel cell anodes II. Steam:carbon ratio and current density. J. Power Sources *277*, 455–463. https://doi.org/10.1016/j.jpowsour.2014.07.084.
37. Muramoto, A., Kikuchi, Y., Tachikawa, Y., Lyth, S.M., Shiratori, Y., Taniguchi, S., and Sasaki, K. (2017). High-pressure C-H-O diagrams: Fuel composition, carbon deposition, and open circuit voltage of pressurized SOFCs. Int. J. Hydrogen Energy *42*, 30769–30786. https://doi.org/10.1016/j.ijhydene.2017.10.122.
38. Broers, G.H.J., and Treijtel, B.W. (1965). Carbon deposition boundaries and other constant parameter curves, in the triangular representation of CHO equilibria, with applications to fuel cells. Adv. Energy Convers. *5*, 365–382. https://doi.org/10.1016/0365-1789(65)90024-X.
39. Halinen, M. (2015). Improving the Performance of Solid Oxide Fuel Cell Systems (VTT Technical Research Centre of Finland). https://aaltodoc.aalto.fi:443/handle/123456789/15748.
40. Peters, R., Deja, R., Blum, L., Pennanen, J., Kiviaho, J., and Hakala, T. (2013). Analysis of solid oxide fuel cell system concepts with anode recycling. Int. J. Hydrogen Energy *38*, 6809–6820. https://doi.org/10.1016/j.ijhydene.2013.03.110.
41. Tsai, T.I., Troskialina, L., Majewski, A., and Steinberger-Wilckens, R. (2016). Methane internal reforming in solid oxide fuel cells with anode off-gas recirculation. Int. J. Hydrogen Energy *41*, 553–561. https://doi.org/10.1016/j.ijhydene.2015.10.025.

42. Yashiro, K., Takase, M., Sato, K., Kawada, T., and Mizusaki, J. (2009). Carbon Deposition and Electrochemical Reaction of Anode for SOFC in Methane Containing Atmosphere. ECS Trans. *16*, 213–218. https://doi.org/10.1149/1.3242236.

43. Wagner, P.H., Wuillemin, Z., Constantin, D., Diethelm, S., Van herle, J., and Schiffmann, J. (2020). Experimental characterization of a solid oxide fuel cell coupled to a steam-driven micro anode off-gas recirculation fan. Appl. Energy *262*, 114219. https://doi.org/10.1016/j.apenergy.2019.114219.

44. Miki, T., Ogawa, N., Nagasaka, T., and Hino, M. (2001). Activity Measurement of the Constituents in Molten Ag-In-Sn Ternary Alloy by Mass Spectrometry. Mater. Trans. *42*, 732–738. https://doi.org/10.2320/matertrans.42.732.

45. Fruehan, R.J. (1970). Activities in Liquid Fe-Al-O and Fe-Ti-O Alloys. In Metallurgical Transactions, p. 8.

46. Zhao, D.g., Guo, P.m., and Zhao, P. (2011). Activity Model of Fe-Si-B Ternary Metallic Melts. J. Iron Steel Res. Int. *18*, 16–21. https://doi.org/10.1016/S1006-706X(11)60071-X.

47. Jaworski, Z., and Pianko-Oprych, P. (2018). A Comparative Thermodynamic Study of Equilibrium Conditions for Carbon Deposition from Catalytic C-H-O Reformates. Energies *11*, 1177. https://doi.org/10.3390/en11051177.

48. Ribeiro, T.R., Ferreira Neto, J.B., Takano, C., Poço, J.G.R., Kolbeinsen, L., and Ringdalen, E. (2021). C-O-H2 ternary diagram for evaluation of carbon activity in CH4-containing gas mixtures. J. Mater. Res. Technol. *13*, 1576–1585. https://doi.org/10.1016/j.jmrt.2021.05.033.

49. Schluckner, C., Subotic, V., Lawlor, V., Hochenauer, C., and Hochenauer, C. (2015). Three-dimensional numerical and experimental investigation of an industrial-sized SOFC fueled by diesel reformat – Part II: Detailed reforming chemistry and carbon deposition analysis. Int. J. Hydrogen Energy *40*, 10943–10959. https://doi.org/10.1016/j.ijhydene.2015.06.024.

50. Sibson, R. (1981). A brief description of natural neighbor interpolation. https://www.semanticscholar.org/paper/A-brief-description-of-natural-neighbor-Sibson/1ca6926bf459db0a4d89a8c88b9fd64c32760bc2.

51. Bartholomew, C.H. (1982). Carbon Deposition in Steam Reforming and Methanation. Catal. Rev. *24*, 67–112. https://doi.org/10.1080/03602458208079650.

52. Gozzi, D., Iervolino, M., and Latini, A. (2007). The Thermodynamics of the Transformation of Graphite to Multiwalled Carbon Nanotubes. J. Am. Chem. Soc. *129*, 10269–10275. https://doi.org/10.1021/ja072120d.

53. Wang, Y., Shi, W., Li, H., Han, M., and Sun, Z. (2019). Long-Term Operation and Post Analysis of a Stack with Methane Fuel. ECS Trans. *91*, 707–718. https://doi.org/10.1149/09101.0707ecst.

54. O'Hayre, R.P., Cha, S.W., Colella, W.G., and Prinz, F.B. (2016). Fuel Cell Fundamentals, Third edition (John Wiley & Sons Inc).

55. Tao, Y., Ebbesen, S.D., and Mogensen, M.B. (2014). Carbon Deposition in Solid Oxide Cells during Co-Electrolysis of H2O and CO2. J. Electrochem. Soc. *161*, F337–F343. https://doi.org/10.1149/2.079403jes.

56. Tu, B., Wang, X., Ou, D., Qi, H., Qiu, P., Zhang, T., Han, S., Cheng, M., and Su, X. (2024). Investigation of limiting H2O/CO2 co-electrolysis to convert renewable electricity into chemical energy using solid oxide electrolysis cell. Renew. Energy *232*, 121040. https://doi.org/10.1016/j.renene.2024.121040.

57. Gozzi, D., Latini, A., and Lazzarini, L. (2009). Experimental Thermodynamics of High Temperature Transformations in Single-Walled Carbon Nanotube Bundles. J. Am. Chem. Soc. *131*, 12474–12482. https://doi.org/10.1021/ja904294z.

58. Sanjabi, S., Faramarzi, A., Hamdam Momen, M., and Barber, Z.H. (2008). Thermodynamics approach of the formation of Ni catalyst particles for carbon nanotubes growth. J. Phys. Chem. Solid. *69*, 1940–1944. https://doi.org/10.1016/j.jpcs.2008.02.003.

59. Muratov, V.B., Vasil'ev, O.O., Kulikov, L.M., Garbuz, V.V., Nesterenko, Y.V., and Duda, T.I. (2012). Thermodynamic properties of multiwalled carbon nanotubes. J. Superhard Mater. *34*, 173–178. https://doi.org/10.3103/S1063457612030045.

60. Jaworski, Z., Zakrzewska, B., and Pianko-Oprych, P. (2017). On thermodynamic equilibrium of carbon deposition from gaseous C-H-O mixtures: updating for nanotubes. Rev. Chem. Eng. *33*. https://doi.org/10.1515/revce-2016-0022.

61. Nakajo, A., Wuillemin, Z., Metzger, P., Diethelm, S., Schiller, G., Van herle, J., and Favrat, D. (2011). Electrochemical Model of Solid Oxide Fuel Cell for Simulation at the Stack Scale I. Calibration Procedure on Experimental Data. J. Electrochem. Soc. *158*, B1083. https://doi.org/10.1149/1.3596433.

62. Nakajo, A., Tanasini, P., Diethelm, S., Van herle, J., and Favrat, D. (2011). Electrochemical Model of Solid Oxide Fuel Cell for Simulation at the Stack Scale II: Implementation of Degradation Processes. J. Electrochem. Soc. *158*, B1102. https://doi.org/10.1149/1.3596435.

63. Sundman, B., Lu, X.G., and Ohtani, H. (2015). The implementation of an algorithm to calculate thermodynamic equilibria for multi-component systems with non-ideal phases in a free software. Comput. Mater. Sci. *101*, 127–137. https://doi.org/10.1016/j.commatsci.2015.01.029.

64. Lewis, G.N., and Randall, M. (1923). Thermodynamics and the Free Energy of Chemical Substances, *38* (McGraw-Hill Book Company Inc).

65. Gibbs, J.W. (1878). On the equilibrium of heterogeneous substances. Trans. Conn. Acad. Arts Sci. *108–248*, 441–458. https://doi.org/10.2475/ajs.s3-16.96.441.

66. Kaufman, L., and Bernstein, H. (1970). Computer calculation of phase diagrams. With special reference to refractory metals vol. 4 of Refractory Materials. A Series in Monographs (Academic Press Inc).

67. Saunders, N., and Miodownik, A. (1998). CALPHAD: Calculation of Phase Diagrams - A Comprehensive Guide Vol. 1 of *Pergamon Materials Series* (Elsevier).

68. Ågren, J. (1982). Numerical Treatment of Diffusional Reactions in Multicomponent Alloys. J. Phys. Chem. Solids *43*, 385–391.

69. Tanaka, T., Hack, K., and Hara, S. (1999). Data to Determine Surface Tension and Viscosity of Metallic Alloys. MRS Bull. *24*, 45–51.

70. Hallstedt, B., Dupin, N., Hillert, M., Höglund, L., Lukas, H.L., Schuster, J.C., and Solak, N. (2007). Thermodynamic models for crystalline phases. Composition dependent models for volume, bulk modulus and thermal expansion. Calphad *31*, 28–37. https://doi.org/10.1016/j.calphad.2006.02.008.

71. Hillert, M. (1981). Some viewpoints on the use of a computer for calculating phase diagrams. Physica B+C *103*, 31–40. https://doi.org/10.1016/0378-4363(81)91000-7.

72. Chen, L.Q. (2019). Chemical potential and Gibbs free energy. MRS Bull. *44*, 520–523. https://doi.org/10.1557/mrs.2019.162.

73. Dinsdale, A. (2009). SGTE Pure Element Database (UNARY), V. 5.0. https://www.sgte.net/en/free-pure-substance-database.

74. Belov, G.V., Iorish, V.S., and Yungman, V.S. (1999). IVTANTHERMO for Windows — database on thermodynamic properties and related software. Calphad *23*, 173–180. https://doi.org/10.1016/S0364-5916(99)00023-1.

75. Kattner, U.R. (2020). The need for reliable data in computational thermodynamics. HTHP *49*, 31–47. https://doi.org/10.32908/hthp.v49.853.

76. Belov, G.V., Dyachkov, S.A., Levashov, P.R., Lomonosov, I.V., Minakov, D.V., Morozov, I.V., Sineva, M.A., and Smirnov, V.N. (2018). The IVTANTHERMO-Online database for thermodynamic properties of individual substances with web interface. J. Phys., Conf. Ser. *946*, 012120. https://doi.org/10.1088/1742-6596/946/1/012120.

77. Lukas, H.L., Fries, S.G., and Sundman, B. (2007). Computational Thermodynamics: The CALPHAD Method (Cambridge University Press).

78. Kattner, U.R. (2016). THE CALPHAD METHOD AND ITS ROLE IN MATERIAL AND PROCESS DEVELOPMENT. TMM *13*, 3–15. https://doi.org/10.4322/2176-1523.1059.

79. Sundman, B., Dupin, N., and Hallstedt, B. (2021). Algorithms useful for calculating multi-component equilibria, phase diagrams and other kinds of diagrams. Calphad *75*, 102330. https://doi.org/10.1016/j.calphad.2021.102330.

80. Davies, C.N. (1984). Gas transport in porous media: The dusty-gas model. J. Aerosol Sci. *15*, 81. https://doi.org/10.1016/0021-8502(84)90058-2.

81. Caravella, A. (2016). Dusty-Gas Model (DGM). In Encyclopedia of Membranes, E. Drioli and L. Giorno, eds. (Springer), pp. 604–605.

82. Rinaldi, G., Nakajo, A., Burdet, P., Cantoni, M., Chiu, W.K.S., and Van herle, J. (2019). Characterization of local morphology and availability of triple-phase boundaries in solid oxide cell electrodes. Acta Mater. *178*, 194–206. https://doi.org/10.1016/j.actamat.2019.07.027.

83. Caliandro, P., Nakajo, A., Diethelm, S., and Van herle, J. (2019). Model-assisted identification of solid oxide cell elementary processes by electrochemical impedance spectroscopy measurements. J. Power Sources *436*, 226838. https://doi.org/10.1016/j.jpowsour.2019.226838.

84. Sandrock, C., and Afshari, S. (2016). alchemyst/ternplot: DOI version. Zenodo. https://zenodo.org/record/166760.

85. Matsuzaki, Y., and Yasuda, I. (2000). Electrochemical Oxidation of H 2 and CO in a H 2 â - H 2 O â - CO â - CO 2 System at the Interface of a Niâ-YSZ Cermet Electrode and YSZ Electrolyte. J. Electrochem. Soc. *147*, 1630. https://doi.org/10.1149/1.1393409.

86. Zhu, H., Kee, R.J., Janardhanan, V.M., Deutschmann, O., and Goodwin, D.G. (2005). Modeling Elementary Heterogeneous Chemistry and Electrochemistry in Solid-Oxide Fuel Cells. J. Electrochem. Soc. *152*, A2427. https://doi.org/10.1149/1.2116607.